Titre: Title:	Biomechanical Modeling of Transforaminal Lumbar Interbody Fusion: A Comparative Assessment of Segmental Lumbar Lordosis and Risk of Cage Subsidence With Different Cage Heights and Placements
Auteur: Author:	Sajjad Rastegar Talzali
Date:	2019
Type:	Mémoire ou thèse / Dissertation or Thesis
Référence: Citation:	Rastegar Talzali, S. (2019). Biomechanical Modeling of Transforaminal Lumbar Interbody Fusion: A Comparative Assessment of Segmental Lumbar Lordosis and Risk of Cage Subsidence With Different Cage Heights and Placements [Mémoire de maîtrise, Polytechnique Montréal]. PolyPublie. https://publications.polymtl.ca/3905/

Document en libre accès dans PolyPublie
Open Access document in PolyPublie

URL de PolyPublie: PolyPublie URL:	https://publications.polymtl.ca/3905/
Directeurs de recherche: Advisors:	Carl-Éric Aubin, & Pierre-Jean Arnoux
Programme: Program:	Génie mécanique

POLYTECHNIQUE MONTRÉAL

affiliée à l'Université de Montréal

Biomechanical Modeling of Transforaminal Lumbar Interbody Fusion: a Comparative Assessment of Segmental Lumbar Lordosis and Risk of Cage Subsidence With Different Cage Heights and Placements

SAJJAD RASTEGAR TALZALI

Département de génie mécanique

Mémoire présenté en vue de l'obtention du diplôme de *Maîtrise ès sciences appliquées*

Génie mécanique

Mai 2019

POLYTECHNIQUE MONTRÉAL

affiliée à l'Université de Montréal

Ce mémoire intitulé :

Biomechanical Modeling of Transforaminal Lumbar Interbody Fusion: a Comparative Assessment of Segmental Lumbar Lordosis and Risk of Cage Subsidence With Different Cage Heights and Placements

présenté par **Sajjad RASTEGAR TALZALI**

en vue de l'obtention du diplôme de *Maîtrise ès sciences appliquées*

a été dûment accepté par le jury d'examen constitué de :

Isabelle VILLEMURE, présidente
Carl-Éric AUBIN, membre et directeur de recherche
Pierre-Jean ARNOUX, membre et codirecteur de recherche
Yvan PETIT, membre

DEDICATION

To my parents and my lovely wife Mahsa,

For your unconditional and genuine love.

ACKNOWLEDGEMENTS

RÉSUMÉ

Les affections pathologiques du rachis lombaire telles que les discopathies dégénératives, les spondylolisthésis ou les hernies discales récurrentes sont connues pour produire des douleurs lombaires et peuvent nécessiter une instrumentation et fusion du rachis dans les cas les plus sévères. La fusion lombaire à l'aide d'un implant intersomatique par voie transforaminale (transforaminal lumbar interbody fusion ou TLIF) est une technique chirurgicale visant à restaurer la hauteur du corps intervertébral, la lordose lombaire segmentaire (SLL), et à accroître la stabilité de la colonne lombaire. La procédure standard implique l'ablation du noyau pulpeux (NP) et d'une partie de l'anneau de cartilage fibreux (AF), suivie de la décompression du segment et de l'insertion d'une cage intersomatique dans l'espace intervertébral par une approche médiolatérale. L'instrumentation postérieure vise en outre à stabiliser et permettre une fusion solide du segment rachidien.

L'une des défaillances mécaniques du TLIF, qui menace le succès de la fusion, est l'affaissement des vertèbres au niveau de la cage et la perte associée de la hauteur du corps vertébral, avec une incidence rapportée entre 8.6 % et 38.1 %. Cet affaissement survient lorsqu'un plateau du corps vertébral ne peut résister aux forces transférées à l'interface plateau vertébral/cage. Bien que des études cliniques, des études expérimentales sur cadavres et des analyses numériques aient été réalisées sur l'utilisation de différentes formes, dimensions, configurations et hauteurs de cage, le rôle des paramètres essentiels de la cage, à savoir sa hauteur et sa position, en lien avec le risque de l'affaissement des plateaux vertébraux n'est pas entièrement compris biomécaniquement.

 L'objectif de ce mémoire était de comparer biomécaniquement les variations angulaires de lordose segmentaire et les risques d'affaissement en utilisant des cages intersomatiques pour différentes hauteurs et positions de cage, ainsi que pour différentes qualités de l'os.

Pour répondre à l'objectif susmentionné, un modèle détaillé par éléments finis (MEF) de l'unité fonctionnelle L4-L5 a été créé sur la base du modèle SM2S (Spine Model for Safety and Surgery), précédemment développé et validé. Ce MEF est basé sur les images tomodensitométriques (épaisseur de coupe de 0.6 mm) d'un homme asymptomatique du 50e percentile. Le MEF comprend les os trabéculaires et corticaux du corps vertébral et des arcs postérieurs, le disque intervertébral, les facettes articulaires et sept ligaments. Le maillage du MEF a été réalisé et vérifié grâce à une étude de convergence et les propriétés des matériaux ont été adaptées de la littérature. L'os

ostéoporotique a été modélisé en réduisant les modules de Young des os cortical et trabéculaire de 33 % et 66 %, respectivement.

Pour simuler la procédure TLIF, on a modélisé la préparation du disque intervertébral en enlevant le NP et les éléments situés à l'arrière gauche de l'AF, puis en enlevant partiellement les éléments correspondants des facettes zygapophysaires de l'articulation. Ensuite, des vis pédiculaires multiaxiales (40 mm x 6.5 mm ; CD HORIZON® LEGACY™ ; Medtronic, USA) ont été insérées sur les deux côtés de chaque vertèbre. Ensuite, une cage (CAPSTONE® interbody cage, Medtronic Inc., Memphis, USA) a été insérée de telle sorte à s'assurer qu'il y avait un contact intime à l'interface plateau vertébral/cage. Ensuite, la fixation postérieure a été réalisée en modélisant deux tiges en titane (4.5 mm) insérées dans les têtes de vis. La surface inférieure de L5 a été immobilisée et le plateau supérieur de L4 a été soumis à une force compressive de 400N orientée selon la courbure spinale, ainsi qu'à des moments de 10 Nm en flexion, extension, flexion latérale et rotation axiale appliquées séquentiellement. Les amplitudes de mouvements et les distributions de contraintes de Von Mises aux interfaces plateau vertébral/cage ont été évaluées. Le changement de SLL après placement de la cage a été calculé comme la différence d'angle entre le plateau supérieur de L4 et le plateau inférieur de L5.

La SLL a été augmentée de 0.9° (11 %) et 1.0° (13 %), respectivement pour la cage de 8 mm en position oblique asymétrique et en position antérieure symétrique ; elle était de 1.4° (18 %) et 1.7° (21 %) en simulant avec une cage de 10 mm de hauteur. La variation de l'amplitude de mouvement après la fixation postérieure simulée était inférieure à 1° pour tous les scénarios TLIF simulés. Par rapport à la cage de 8 mm, les contraintes maximales aux interfaces plateau vertébral/cage de 10 mm étaient jusqu'à 16 % plus élevées dans les simulations avec le modèle osseux normal, comparativement à celui ostéoporotique. Les contraintes maximales pour le placement asymétrique de la cage étaient respectivement jusqu'à 41 % et 43 % plus élevées que le placement symétrique avec le modèle osseux normal vs. ostéoporotique.

Pour une qualité osseuse normale simulée, avec l'utilisation d'une cage de 8 mm, les contraintes maximales à l'interface plateau vertébral/cage variaient de 82.1 à 98.4 MPa (placement symétrique antérieur) et de 117.9 à 155.5 MPa (placement asymétrique oblique). Avec l'utilisation d'une cage de 10 mm, elles étaient de 88.2 à 107.2 MPa (placement symétrique antérieur) et entre 134.4 et 176.4 MPa (placement asymétrique oblique). Pour la simulation de l'os ostéoporotique, les

contraintes à l'interface plateau vertébral/cage étaient inférieures d'environ 2.5 %. Le placement oblique asymétrique par rapport au placement antérieur symétrique de la cage a augmenté les contraintes maximales à l'interface plateau vertébral/cage jusqu'à 41 % et 43 % respectivement pour l'os normal et l'os os ostéoporotique simulé. L'insertion de la cage de 10 mm par rapport à celle de 8 mm a augmenté les contraintes maximales à l'interface plateau vertébral/cage jusqu'à 16% pour le modèle osseux normal vs. ostéoporotique. Les contraintes dans les tiges postérieures ont augmenté jusqu'à 120% pour la simulation de l'os ostéoporotique. Le placement oblique asymétrique par rapport au placement antérieur symétrique de la cage a augmenté les contraintes maximales dans les tiges postérieures jusqu'à 55% et 48% pour l'os normal et ostéoporotique simulé, respectivement. L'insertion de la cage de 10 mm par rapport à celle de 8 mm a augmenté les contraintes maximales dans les tiges postérieures jusqu'à 59% et 54% respectivement pour le modèle osseux normal vs. ostéoporotique.

La SLL résultante était plus élevée avec la cage de 10 mm qu'avec la cage de 8 mm pour chaque stratégie de placement. La SLL simulée en placement asymétrique oblique était identique à celle du placement symétrique antérieur. Les contraintes maximales augmentaient avec le placement asymétrique oblique et l'utilisation d'une cage de 10 mm, ce qui est interprété comme favorable à l'augmentation du risque d'affaissement des plateaux vertébraux. Comme l'os ostéoporotique a des propriétés mécaniques réduites, le risque d'affaissement de la cage devrait être plus élevé. Les contraintes maximales dans les tiges postérieures étaient plus élevées en position oblique asymétrique et avec l'utilisation d'une cage de 8 mm. De plus, avec l'ostéoporose simulée, les contraintes maximales dans les tiges postérieures ont augmenté, ce qui peut impliquer un risque plus élevé de défaillance des tiges.

ABSTRACT

Pathological conditions such as degenerative disc disease, spondylolisthesis, or recurrent disc herniation are known to produce back pain and may be indications for a lumbar spinal fusion for disabling low back conditions that were unsuccessfully improved with non-surgical treatments. Transforaminal lumbar interbody fusion (TLIF) is a surgical technique to restore the intervertebral body height, the segmental lumbar lordosis (SLL), and to add stability to the lumbar spine. The standard procedure involves the removal of the nucleus pulposus (NP) and a portion of the annulus fibrosus (AF), followed by decompression of the segment and insertion of the interbody cage into the intervertebral disc space through a mediolateral approach. Posterior instrumentation additionally aims to achieve a solid fusion at the spinal segment.

Cage subsidence is one of the mechanical failures of TLIF which threatens the success of the spine fusion with a reported incidence between 8.6% and 38.1%. Cage subsidence is a situation where an endplate fails to withstand the transferred loads at the endplate-cage interface resulting in the loss of the intervertebral body height. Although clinical studies, cadaveric experimental investigations, and numerical analyses have investigated the use of different cage shapes, dimensions, configurations, and heights, the role of essential cage parameters, namely the height of cage and its placement strategy, in the risk of cage subsidence are not fully biomechanically understood. The objective of this project was to biomechanically assess the resulting SLL and stresses at the endplate-cage interface with the change of the cage height, its placement strategy, and the bone quality.

To address the aforementioned objective, a detailed finite element model (FEM) of the L4-L5 functional unit was created based on the previously developed and validated Spine Model for Safety and Surgery (SM2S) FEM. The FEM of the L4-L5 functional unit is based on the CT-scan images (0.6 mm slice thickness) of a 50th percentile asymptomatic man. The FEM includes trabecular and cortical bones of the vertebral body and of the posterior processes, the intervertebral disc, the facet joints, and seven ligaments. The FEM was properly meshed and refined through a convergence study and material properties were adapted from the literature. Osteoporosis was modeled by reducing the Young's modulus of the cortical and trabecular bones by 33% and 66%, respectively.

To simulate the TLIF procedure, intervertebral disc preparation was modeled by removing the NP and elements at the posterior-left of the AF followed by partial removal of the corresponding elements of the zygapophyseal facet joints. Next, multiaxial pedicle screws (40 mm x 6.5 mm; CD HORIZON® LEGACY™; Medtronic, USA) were inserted on two sides of each vertebra. Then, an available cage (CAPSTONE® interbody cage, Medtronic Inc., Memphis, USA) was inserted in such a way there was an intimate contact at the endplate-cage interface. After, the posterior fixation was performed by modeling two titanium rods (4.5 mm) aligned with the screw head saddle. The simulated TLIF model was subjected to a 400 N follower load and a 10-Nm bending moment simulating the functional loads in the three anatomical planes to mimic flexion (Fe), extension (Ex), right lateral bending (RLB), left lateral bending (LLB), right axial rotation (RAR), and left axial rotation (LAR). Two cage heights (8 and 10 mm), two placement strategies (anterior symmetric vs. oblique asymmetric) were tested for two simulated bone qualities (normal and osteoporotic). The range of motion (ROM) and maximum Von-Mises stresses at the endplate-cage interface as the predictor of the risk of cage subsidence were calculated. The change of the SLL after cage placement was calculated as the difference of angle between the superior endplate of L4 and the inferior endplate of L5.

The SLL was increased by 0.9° (11%) and 1.0° (13 %), respectively in oblique asymmetric and anterior symmetric cage placement with 8-mm cage height; they were 1.4° (18%) and 1.7° (21 %) when simulating with a 10-mm height cage. The change in the range of motion after the simulated posterior fixation was lower than 1° in all the simulated TLIF scenarios. Compared to the 8-mm cage, maximum stresses at the cage-bone interface with the 10-mm cage were up to 16% higher in simulations with both normal and osteoporotic bone models. Maximum stresses in asymmetric cage placement were respectively up to 41% and 43% higher than the symmetric placement in normal and osteoporotic bone models.

For simulated normal bone quality, with the use of 8-mm, the maximum stresses at the bone-cage interface ranged from 82.1 to 98.4 MPa (anterior symmetric placement) and from 117.9 to 155.5 MPa (oblique asymmetric placement). With the use of 10-mm cage, they were from 88.2 to 107.2 MPa (anterior symmetric placement) and between 134.4 and 176.4 MPa (oblique asymmetric placement). For the simulated osteoporosis, stresses at the bone-cage interface were about 2.5% lower. Oblique asymmetric vs. anterior symmetric cage placement increased the maximum stresses at the endplate-cage interface up to 41% and 43% for the simulated normal and osteoporotic bone,

respectively. Insertion of the 10-mm cage vs. the 8-mm one increased the maximum stresses at the endplate-cage interface up to 16% in simulated normal and osteoporotic bone models. Stresses in the posterior rods increased up to 120% with osteoporosis bone. Oblique asymmetric vs. anterior symmetric cage placement increased the maximum stresses in the posterior rods up to 55% and 48% for the simulated normal and osteoporotic bone, respectively. Insertion of the 10-mm cage vs. the 8-mm one increased the maximum stresses in the posterior rods up to 59% and 54% in simulated normal and osteoporotic bone models, respectively.

The resulting SLL was higher with the 10-mm cage vs. 8-mm in each placement strategy. The simulated SLL in oblique asymmetric placement was identical to that of anterior symmetric placement. The maximum stresses increased with the oblique asymmetric placement and the use of 10-mm cage which may increase the risk of cage subsidence. Since osteoporotic bone has compromised mechanical properties, the risk of cage subsidence should be higher though the maximum stresses at the endplate-cage interface were similar for those bone qualities. The maximum stresses in the posterior rods were higher in oblique asymmetric placement and with the use of 8-mm cage. Also, with the simulated osteoporosis, the maximum stresses in the posterior rods increased, which may imply a higher risk of failures of the rods.

TABLE OF CONTENTS

LIST OF TABLES

LIST OF FIGURES

LIST OF SYMBOLS AND ABBREVIATIONS

ρ	Density
λ_0	Navier's constant
ν	Poisson's ratio
ν_r	Tangent poisson's ratio
η_0	Viscosity coefficient
1F	1 mm shift in position of oblique asymmetrically placed 10-mm cage toward anterior
1L	1 mm shift in position of oblique asymmetrically placed 10-mm cage toward left
1B	1 mm shift in position of oblique asymmetrically placed 10-mm cage toward posterior
1R	1 mm shift in position of oblique asymmetrically placed 10-mm cage toward right
A08	Oblique asymmetric placement of the 08-mm cage
A10	Oblique asymmetric placement of the 10-mm cage
AF	Annulus fibrosus
ALIF	Anterior lumbar interbody fusion
ALL	Anterior longitudinal ligament
ASD	Adjacent segment degeneration
CAD	Computer aided design
CL	Capsular ligament
E	Elastic modulus
Ex	Extension
E_r	Tangent modulus
EZ	Elastic zone
Fe	Flexion
FE	Finite element
FEA	Finite element analysis
FEM	Finite element model
ILS	Interspinous ligament
ITL	Intertransverse ligament
LAR	Left axial rotation
LF	Ligament flavum
LLB	Left Lateral bending
NP	Nucleus Pulposus

NZ   Neutral zone

PLIF   Posterior lumbar interbody fusion

PLL   Posterior longitudinal ligament

RAR   Right axial rotation

RLB   Right lateral bending

ROM   Range of motion

SSL   Supraspinous ligament

S08   Anterior symmetric placement of the 08-mm cage

S10   Anterior symmetric placement of the 10-mm cage

TLIF   Transforaminal lumbar interbody fusion

XLIF   Lateral lumbar interbody fusion

CHAPTER 1   INTRODUCTION

Degenerative disc diseases such as spondylolisthesis, disc herniation, and lumbar spine stenosis are known to produce low back pain. Worldwide, 266 million people (3.63%) per year suffer from low back pain, which places a burden on the socioeconomic systems [1]. Some of the pathological situations associated with low back pain may have the indications for a lumbar spinal fusion when disabling low back conditions are unsuccessfully improved with non-surgical treatments.

Transforaminal lumbar interbody fusion (TLIF) is a surgical intervention used in spinal deformity, iatrogenic instability, and degenerative disc diseases [2]. TLIF restores the anterior column stability by the means of interbody cages, while the posterior instrumentation further re-establishes support to the functional unit, leading to a solid fusion [2, 3]. After patient positioning and level exposure, the surgeon places the pedicle screws and prepares the intervertebral disc space followed by the decompression of the segment. Thereafter, the interbody cage is inserted through the unilateral approach into the intervertebral disc space, and the rods, which are connected to the pedicle screws, provide additional stability. Interbody cages come in a variety of shapes (bullet shape, kidney (moon)-shape, and articulating semilunar), geometries (height or thickness, width, and footprint), and profile of the faces in contact with the endplates (flat or biconvex) to enhance the rate of fusion in TLIF.

Cage subsidence is a mechanical postoperative complication associated with the TLIF, a situation in which endplates collapse and interbody cage enters the vertebral body. This situation with the reposted rate of 8.6% to 38.1% [4-6] leads to the loss of restored lumbar lordosis (LL) and disc height. Many parameters associated with the risk of cage subsidence have been identified, such as the cage geometry (shape and size) [5, 7-12], single vs. paired cages [13], and the use of unilateral vs. bilateral posterior fixation [14, 15].

Finite element analyses (FEA) showed that 75% larger footprint of the cage (e.g. 490 vs. 280 mm^2) not only increased the physiological load bearing of the anterior segment by about 300%, but also reduced the maximum stresses in the endplate-cage interface by about 50% resulting in a lower risk of cage subsidence [7]. Cadaveric experimental tests demonstrated that although the cages possessing the biconvex faces can better fit into the intervertebral disc space, they tended to concentrate the load in the medial region of endplates with relatively lower mechanical strength (as compared to the peripheral region), thus increasing the risk of cage subsidence [11]. Single cage

insertion generated 77 MPa maximum stress at endplate-cage interface, while it was reduced to 50 MPa with paired-cages (about 55% of lower maximum stress) [13]. Using unilateral pedicle screw fixation in contrast to the bilateral screws increased the maximum stresses at the fused segment up to 45% and in the screw up to 85% [15].

From a mechanical standpoint, using a cage with greater height is more effective for the restoration of the segmental lumbar lordosis (SLL), but it requires more intervertebral distraction resulting in the increased compressive force at the endplate-cage interface. A cadaveric study demonstrated that the measured compressive force at the endplate-cage interface with a 6-mm cage was 8.8 N and raised to 21.5 N with 8-mm cage [16]. Clinical studies proved that 16% more anterior placement of a kidney-shape cage vs. a medial placement of a bullet-shape cage resulted in higher SLL restoration up to 2.11^0 [17], and shifted the endplate-cage contact to the peripheral region of the cortical bone with higher mechanical strength. Using wedged cages (vs. flat or parallel cages) are reported to allow better lordosis restoration; increasing the wedge angle from 4° to 15° improved the resulting SLL from 2.6° to 6.5° [18].

To date, several clinical studies, cadaveric experimental tests, and numerical analyses have been devoted to comprehending the biomechanics of cage subsidence in TLIF. Several risk factors of cage subsidence in TLIF have been identified, such as the cage geometry (shapes and sizes), single cage vs. paired cages, and the use of unilateral posterior fixation vs. bilateral one. Furthermore, clinical observation showed that a thicker cage allows better SLL restoration, although it increases the compression loads at the endplate-cage interface leading to a higher risk of cage subsidence. The anterior placement of the cage is clinically proven to have a lower risk of cage subsidence. Moreover, osteoporosis impairs the bone quality resulting to a compromised mechanical bone strength. Although these findings have contributed to the knowledge of TLIF surgeries, cage subsidence remains an important problem. The objective of this project was to biomechanically assess the resulting SLL and the maximum stresses at endplate-cage interface in TLIF as functions of the cage height, its placement strategy, and the bone quality.

This master thesis is divided into six chapters. The first chapter presents a critical review of the literature and includes a description of the related anatomy and biomechanics of the spine, a review of modeling techniques, and frontier studies related to TLIF. The second chapter presents the research question, related objectives, and the rationality behind the study. The third chapter

encloses a manuscript submitted to a peer-reviewed journal (*Medical & Biological Engineering & Computing*), which includes the key contribution of this thesis. Chapter four presents supplementary tests to establish credibility of the developed FEM and the obtained results. Chapter five presents a general discussion, the limitations of this study, and the perspectives. Finally, chapter six provides a conclusion and recommendations out of this project.

CHAPTER 2   LITERATURE REVIEW

2.1   Anatomy of human spine

The spinal column is a musculo-skeletal system of the human body that connects the upper limbs to the lower body and protects the spinal cord. It is composed of alternating vertebrae and intervertebral discs (IVDs) supported by the robust ligaments and muscles. The asymptomatic spine is straight in the frontal plane, while it has two lordotic and two kyphotic curves in the sagittal plane with five particular segments including the cervical, thoracic, lumbar, sacrum, and coccyx regions (Figure 2-1). The cervical spine is composed of seven vertebrae (C1-C7) and has an arch convex anteriorly in the sagittal plane, known as cervical lordosis. This region of the spine supports the weight of the head and provides mobility. The thoracic spine encompasses twelve vertebrae (T1-T12) with an anteriorly concave curvature in the sagittal plane, denoted by thoracic kyphosis. The lumbar spine includes five vertebrae (L1-L5) and forming a lordosis. The lumbar spine forms the lumbosacral curve, which supports the body weight and maintains the spinal balance. The sacrum (S1-S5) and coccyx (Co1-Co4) are made of fused vertebrae and together form a kyphotic shape in the sagittal plane. The sacrum is a part of pelvis linking the lumbar spine to the lower limbs. The coccyx, or tailbone, is attached to the end of the sacrum and plays a role in the load bearing, especially in sitting.
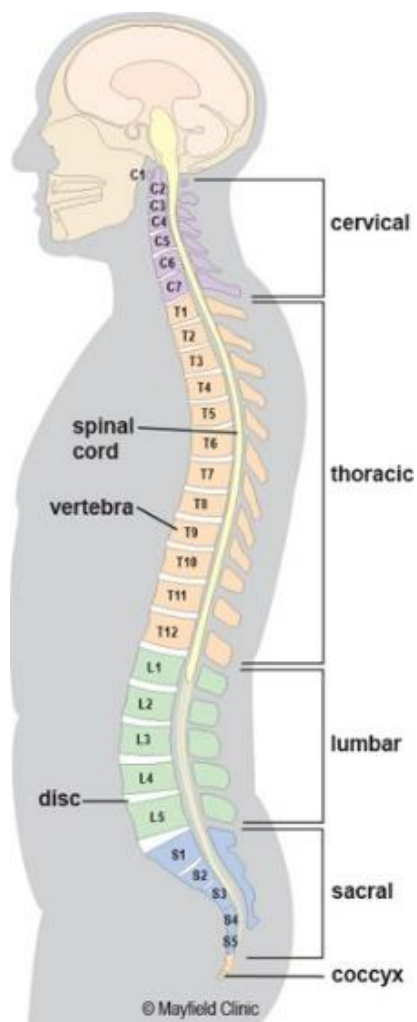
Figure 2-1 Natural spinal curves and different regions of the spinal column (obtained from https://www.mayfieldclinic.com/PE-AnatSpine.htm on 2018-03-12)

2.1.1 Vertebrae

The vertebrae are the main building blocks of the spine and are connected by the spinal ligaments and intervertebral discs that form a coiled spring structure. This arrangement helps to bear the majority of the weight, to serve the mobility to the upper body as well as to protect the spinal cord. Each vertebra has two major parts: (1) the anterior vertebral body, and (2) the posterior part denoted as the neural arch. The vertebral body is the largest part of a vertebra; it has a drum shape that plays a significant role in bearing the loads and withstanding against the compression. In terms of morphology, the vertebral body is generally composed of porous trabecular bone surrounded by a

thin layer of cortical bone, which serves the load bearing ability. The neural arches are bony projections in the back of the vertebrae and are composed of two pedicles, two laminae, two transverse processes, one spinous process, and four facet joints. The vertebral body and neural arches form a central vertebral foramen, which creates a vertebral canal to protect the spinal cord. The superior and inferior notches of the adjacent pedicles construct the intervertebral foramina, through which the spinal nerves pass (Figure 2-2).
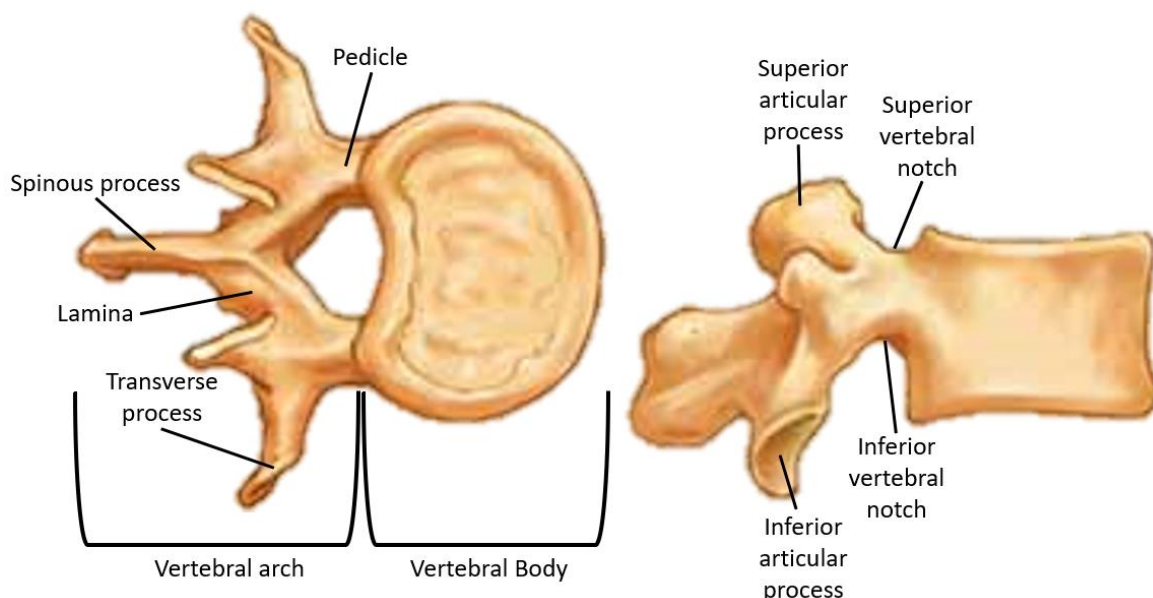
Figure 2-2 General structure of a typical lumbar vertebra. Each vertebra has generally two particular parts including the vertebral body and posterior arches. (Modified picture taken from http://craftbrewswag.info/lumbar-vertebrae/ on 2018-03-13)

2.1.2 Intervertebral discs

The intervertebral discs (IVDs) lie between two adjoining vertebrae and connect them together. They provide the load bearing and shock absorption ability while offering the mobility to the spine. The IVD has a fibrocartilaginous construct and is composed of two parts: the nucleus pulposus (NP) and annulus fibrosus (AF). The core of the intervertebral disc, i.e. NP, is a fluid-like jelly material embedded in composite-like material of AF (Figure 2-3-A).
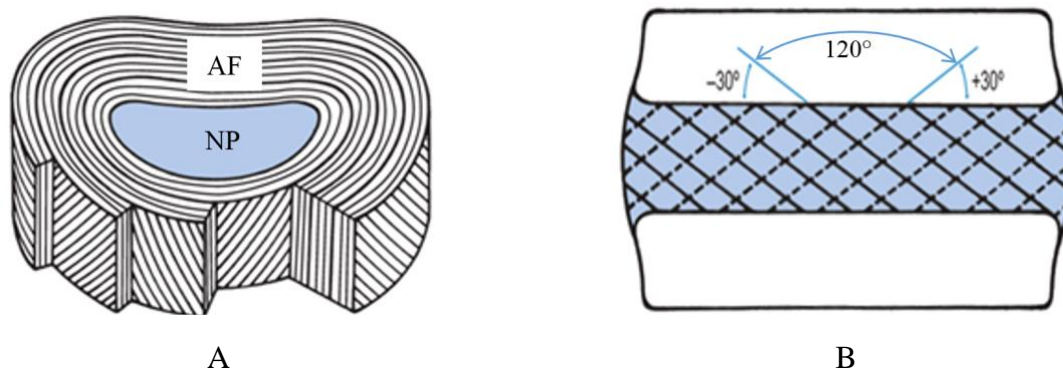
Figure 2-3 Structure of the intervertebral disc, A) NP and AF composed of concentric layers, B) Orientation of collagen fibers of the AF [19]

Water content in the adult healthy disc is approximately between 70% and 80% [20], but it can decrease due to disc degeneration, so called disc dehydration. The AF is a ground material filled with obliquely oriented collagen fibers at about 30°. Collagen fibers are arranged in 15-25 concentric sheets [19] known as lamellae. They are oriented in a reverse direction between two adjacent layers with an angle around 120° (Figure 2-3-B).

2.1.3 Ligaments

The spinal ligaments are connective tissues holding vertebrae together along the spinal column to stabilize the spine and protect the IVDs. There are seven major ligaments, including the anterior longitudinal ligament (ALL), posterior longitudinal ligament (PLL), capsular ligaments (CL), ligamentum flavum (LF), interspinous ligaments (ISL), supraspinous ligaments (SSL), and intertransverse ligaments (ITL). They run from the base of the skull to the sacrum and prevent the excessive flexion, extension, and rotation in each segment (Figure 2-4).

The ALLs are the thick ligaments passing the anterior part of the spine. These ligaments are attached to the adjacent endplates and IVDs, thus preventing the hyperextension of the spine, and avoiding the disc herniation. The PLLs are also lining the posterior side of the vertebral bodies inside the spinal canal to restrict against the posterior prolapse and disc protrusion. The CLs bind

the adjacent superior and inferior articular processes and enclose the articular facet joints. These ligaments have the major contribution to the resistant forces in flexion of the spine. The LFs connect each two adjacent laminae and are highly elastic compared to the other spinal ligaments. The key role of these ligaments is to assist straightening of the flexed spine, to restrict the separation of two adjacent laminae, and to protect the spinal cord. The ISLs are between two neighbouring spinous processes, while the SSLs link their rips. Together, SSLs and ISLs restrict the hyperflexion of the spine. The ITLs are discontinues, connecting two adjoining transverse processes, and contributing to the stability of the spine in lateral bending.
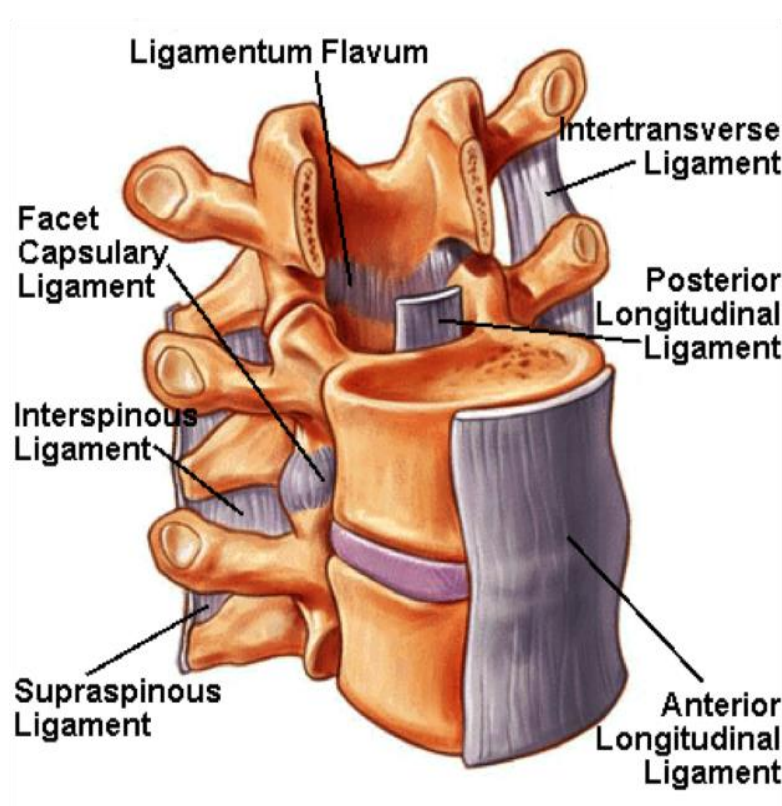
Figure 2-4 Seven spinal ligaments (Taken from: https://www.studyblue.com/notes/note/n/neck-trunk/deck/10491924 on 2018-03-13)

2.2 Biomechanics of the asymptomatic spine

2.2.1 Spinal loads

The spinal column is the main structure sustaining the loads in the musculoskeletal system while providing sufficient flexibility to the upper body [21]. The spinal loads are generated by the spinal muscles and soft tissues to counteract the exerted moments and loads to the spine as well as gravity [21, 22]. Physiological loads are generated in daily movements such as bending, sitting, standing, walking, running, and jumping, but the fast and dynamic movements produce significantly higher magnitude loads. *In vivo* measurements of the intradiscal pressure (between 0.98 to 1.47 MPa) in the sitting posture indicate the role of the IVDs as a load bearing component in the spine [23]. The transferred loads to the FSUs are indicators that could be used to assess the risk of spinal injury or failure, however, they cannot solely determine either the tissue damage or source of pain [22].

The spinal muscles, ligaments, and intra-abdominal pressure (IAP) collectively preserve the stability of the spine [22, 24]. Muscle forces, governed by the nervous system, not only stabilize the spine in upright standing, but also promote and control the movements [22]. In addition to the muscle forces, spinal ligaments and articular joints constrain the extreme movement of the spine. When the muscle and ligament forces increase, the intra-abdominal pressure rectifies the tension along the spine, which moderate the extra compression by generating a hydrostatic pressure on the pelvic and diaphragm [22, 25-27]. The intradiscal L3-L4 pressure measured as a function of posture showed that sitting vs. standing can increase the pressure about 2 times [23]. In lifting an object, the weight, size, lifting speed, and lifting technique would directly affect the spinal loads [24]. Intra-abdominal pressure and muscles contraction may compensate a portion of excessive loads generated by a poor lifting technique. In dynamic activities, the spinal loads are added by the inertial forces and are correlated to the speed and posture [24, 28].

Quantification of the spinal loads generated by the gravity and muscles forces is limited by the available measurements. Schultz et al. [29] proposed to simulate the body weight in numerical simulations by allocating 14% body weight to T1 with the segmental increment of 2.6% toward L5. In order to take the center of mass of the vertebra into account, Clin et al. [30 1880] adapted this load approximation technique and applied a shift to the point of action of each equivalent load in the sagittal plane. Applying a compressive vertical load to each motion segment for the purpose

of gravity force mimicking led to the buckling of the spine in a load magnitude even 10 times lower than the physiological loads [31]. Application of a "follower load" has been widely used in the biomechanical studies to minimize the effect of the shear forces at a motion segment. A follower load can be applied through the curvature of each motion segment in numerical studies, and might be integrated by using a wire-guide system in experimental studies [31].

2.2.2 Spinal Motion

Spinal motion is made by the interaction of spinal elements that allows one vertebra in a motion segment to rotate and translate with respect to the adjacent vertebra. The spinal load-deformation behavior of the motion segment can be characterized to evaluate its stiffness in different loading conditions. This curve has a non-linear behavior with apparently two distinguished regions (Figure 2-5). The first region, the neutral zone (NZ), has a relatively large deformation for a low applied force due to the laxity of the IVDs and spinal ligaments. The next stiffer zone, elastic zone (EZ), is beyond the neutral zone up to the maximum physiological limit. The range of motion (ROM) is the summation of these two regions that, indeed, is the movement of the spinal segment from neutral position up to the limit of motion [24, 32]. The neutral zone is an interesting indicator to assess the spine health, since injuries, degeneration, and surgical intervention could modify the ROM (Figure 2-6).
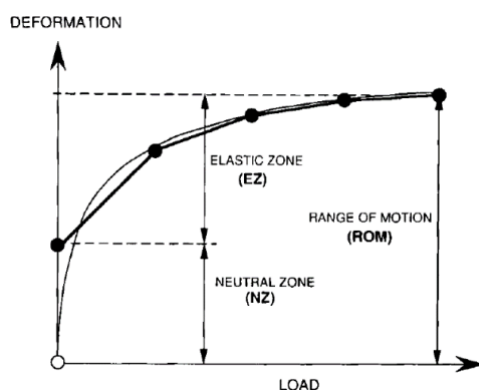
Figure 2-5 A typical load-deformation curve of a joint, e.g. between two adjacent vertebrae, has two major regions: the flexible region at low load called neutral zone (NZ); and stiff region called elastic zone (EZ). NZ and EZ together provide the range of motion (ROM) [33]
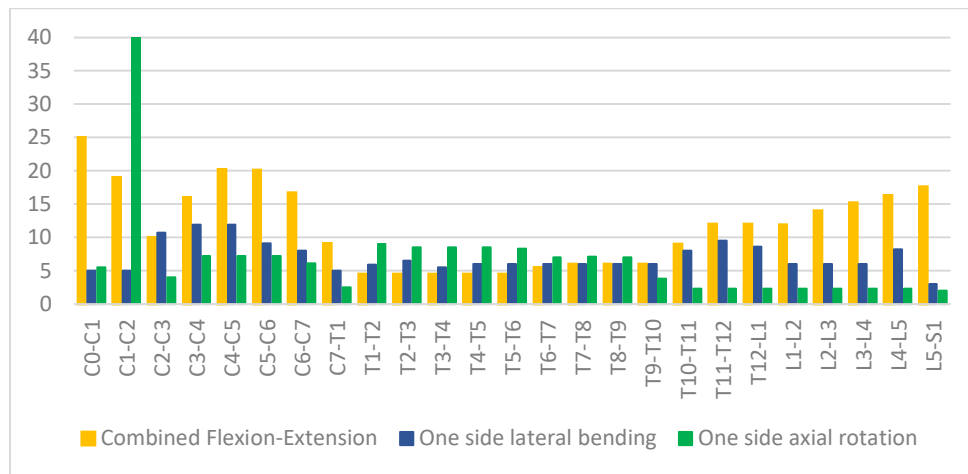
Figure 2-6 Segmental range of motion for each spinal segment in flexion-extension, side bending, and axial rotation summarized from [32]

The spinal movement has two substantial components: rotation around and translation along the anatomical axes (Figure 2-7). Forward and backward rotations around the sagittal axis (Y) are known as flexion and extension, respectively. Lateral bending and axial rotation refer to the rotation around the coronal (X) and transverse (Z) axes, respectively.
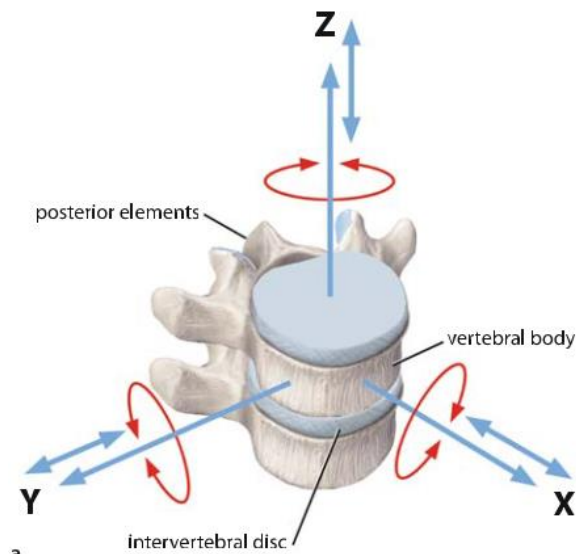
Figure 2-7 Each spinal segment provides six degrees of freedom (DOFs): three translations and three rotations (Image taken from [24])

2.3 Spinal pathologies with the disc as the source of mechanical back pain

Intervertebral disc degeneration (DDD for degenerative disc disease) is the change in the structure and function of the disc, and is initiated by aging or mechanical overloading [34]. Early age-related degeneration often starts off in the NP and reaches the AF [22]. Water content and proteoglycans concentration are respectively 88% and 65% of the dry weight of an asymptomatic disc, and respectively decrease to 65% and 16% with degenerative pathologies [35]. As the NP loses its water content or the AF becomes weak, the IVD collapses and places a pressure on the nerve roots. This situation may lead to the spinal instability and cause the back pain.

One of the most common disc diseases is disc herniation, a situation when gel-like material of the NP leaks out and induces a pressure on the nerve roots. Loss of the nucleus function causes an abnormal force to the AF and initiates the micro-tears in the AF, lamellae, or near the endplates [36]. Overloading the spine may yield the encased NP to escape the AF. This prolapsed material may place a pressure on the nerve roots and cause irritation. The disc degeneration may progress until the destruction of the soft tissues constraining the FSU [20]. Based on the radiological and morphological assessments, Thompson et al (1990) [37] proposed a classification of the disc degeneration from grade I to V. Grade I is corresponding to the healthy disc with rounded nucleus, while the intervertebral disc space collapses in grade V (Figure 2-8).
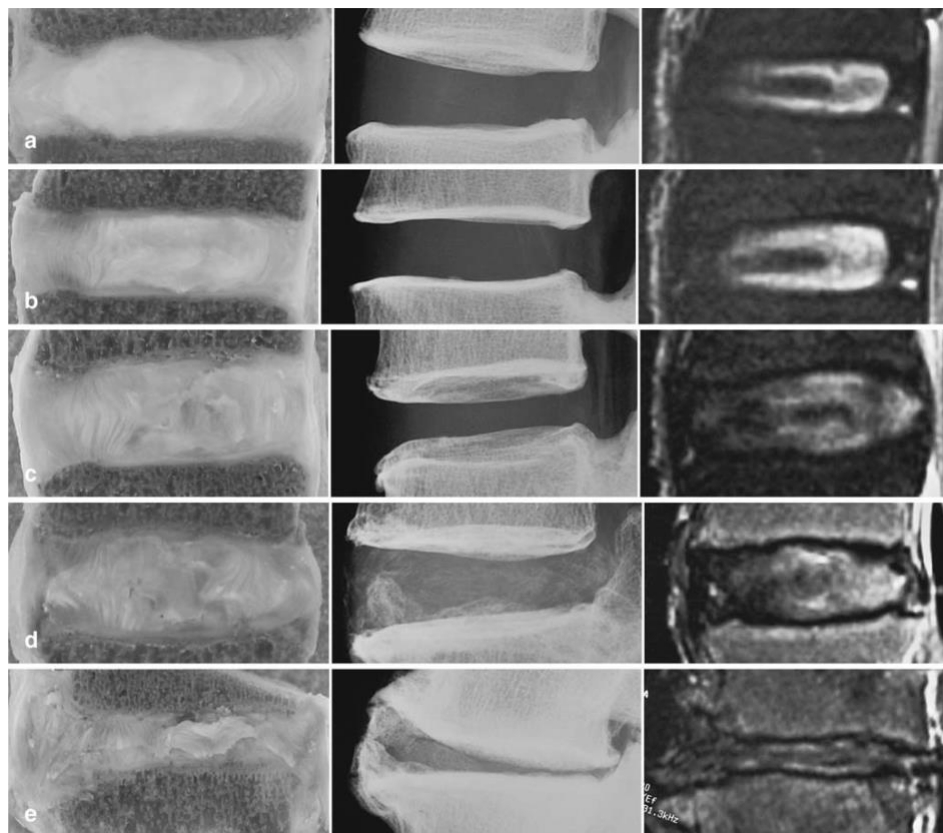
Figure 2-8 Classification of disc degeneration proposed by Benneker et al. (2005) [38]. From grade I (a) to grade Ⅴ (e), the severity increased based on the evaluation of radiological parameters such as disc height, nucleus roundness, and colors

2.4 Transforaminal lumbar interbody fusion (TLIF)

Spinal fusion is a surgical treatment to restore the disc height and segmental lordosis, as well as to increase the stability of the spine. The procedure includes removal of the NP and a portion of the AF, intervertebral disc, partial facetectomy, segment decompression, and insertion of an interbody cage into the intervertebral space. In addition to the cage insertion at the anterior column, a posterior instrumentation brings further solidity to the FSU. To achieve the surgical objective, several techniques are proposed (Figure 2-8):

- anterior lumbar interbody fusion (ALIF) considers an anterior abdominal approach to access to the intervertebral disc space;
- posterior lumbar interbody fusion (PLIF) to access to the disc space with a posterior incision;
- transforaminal lumbar interbody fusion (TLIF) is an unilateral approach to implant the interbody cage.
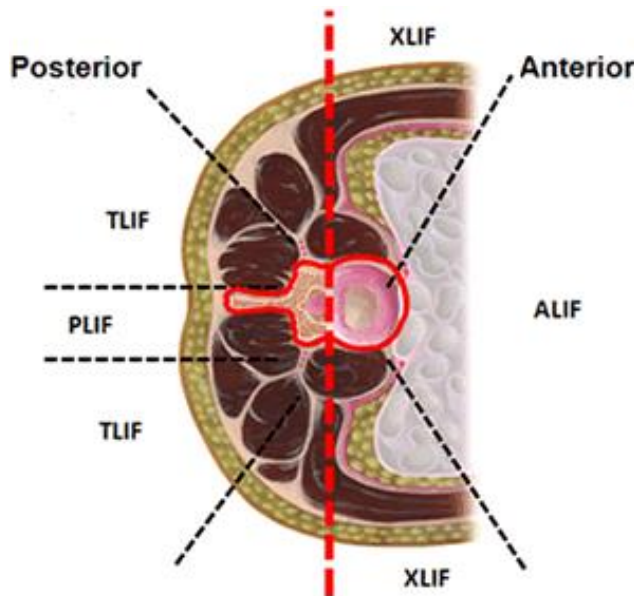
Figure 2-9 Common surgical fusion approaches (Image taken and modified from https://pbrainmd.wordpress.com/2015/10/11/lumbar-interbody-fusion/ on 2018-03-13)

2.4.1 Description of TLIF procedures

Transforaminal lumbar interbody fusion (TLIF) uses the unilateral mediolateral approach to access the intervertebral disc space [2]. The TLIF procedure is presented in the Figure 2-10 according to the standard practice reported in the literature [2, 3]. To access the disc space, the patient is placed in the prone position on a surgical frame. A vertical incision is made over the segment undergoing the fusion. Then, the surgeon retracts the muscles and soft tissues to reach the spinous process, the lamina, and the facet joint. Depending on the type of pathology and required decompression, laminectomy and/or facetectomy may be carried out.

After primary decompression of the nerve roots, pedicle screws are inserted according to the standard procedure. To reach the intervertebral disc space and perform discectomy, the segment may be distracted by using pedicle screws and distractor tools. Discectomy should be carefully performed by removal of the NP and inner layers of AF, while the outer layers of the latter are kept to retain the bone graft after cage placement. Next, the appropriate cage (size) is inserted between two endplates and the rest of intervertebral space is filled with bone graft. After anterior stabilization and restoration of the disc height, rods are placed, and pedicle screws become tighten to achieve the desired lordosis angle (Figure 2-11). Compared to the ALIF, TLIF requires less retroperitoneal dissection with lower risk to damage the large blood vessel going to the legs; TLIF also necessitates less perineural retraction than PLIF [2, 39, 40].

Different interbody cages are available for the TLIF surgical intervention. Cage variations include the material (auto-graft iliac crest, allograft bone, carbon fiber cages, titanium mesh cages, polyether ether ketone (PEEK), and n-HA/PA66), the geometry (footprint, height, and other dimensions), the general shape (bullet or banana- shape vs. straight cages), the morphology of the surfaces in contact with the endplates (flat vs. biconvex), and the cage angle (wedge vs. flat or parallel) (Figure 2-12).
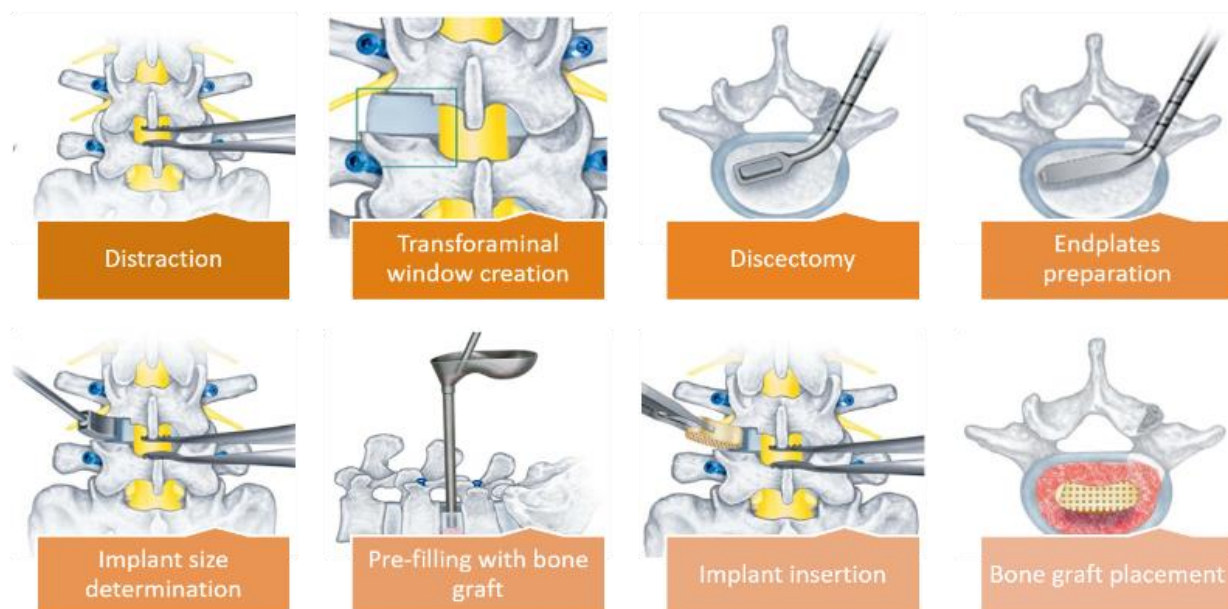
Figure 2-10 The detailed procedure of TLIF

Figure 2-11 The lumbar spine underwent single level TLIF (Image taken from http://img.medicalexpo.com/images_me/photo-g/79814-4109787.jpg on 2018-03-13)
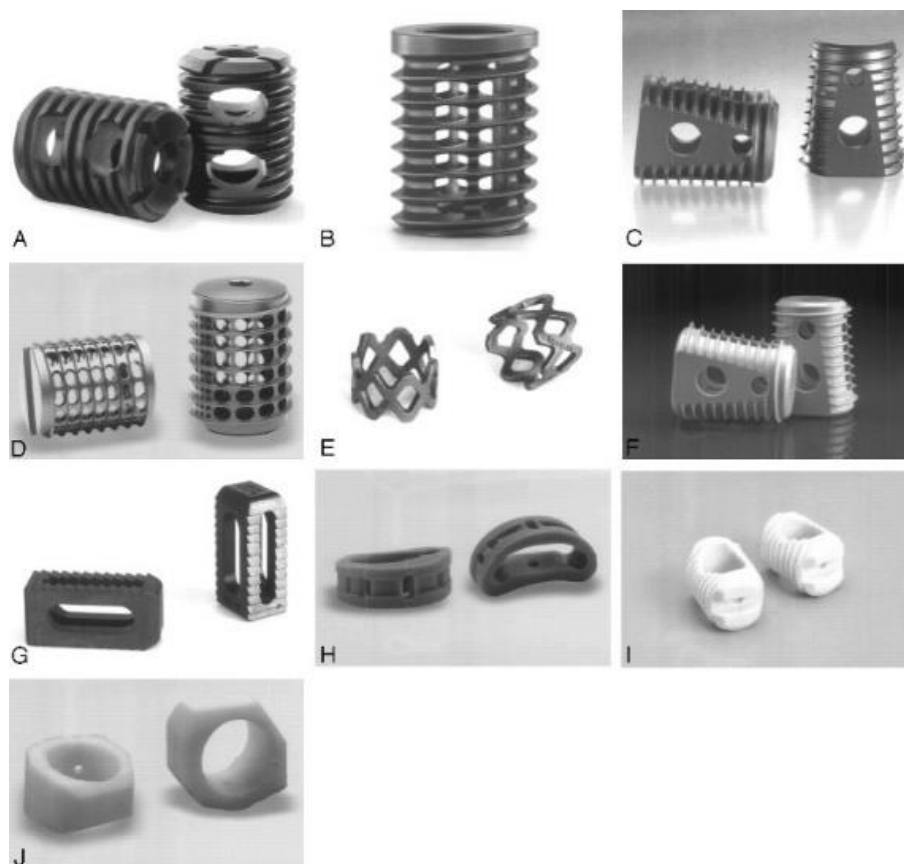
Figure 2-12 Interbody cages with different shapes and materials (Image taken from [41])

2.4.2 Biomechanics of TLIF

TLIF aims to restore the intervertebral disc height and lumbar lordosis, to maintain the achieved stability by the means of interbody cages in anterior column and posterior instrumentation. Mechanical strength of the implant, its durability under cycling loads (fatigue strength), and its capability to restore the sagittal balance are three key features to assess the performance of the spinal instrumentation [42]. Since each pathologic condition has its own nature, the appropriate implant and instrumentation technique are required to assure the proper stability of the spine. The complications associated with the pedicle screws for the spinal fusion when utilizing only posterior instrumentation are attributed to the lack of anterior column stability [43]. It was shown that the use of interbody cages and posterior instrumentation in TLIF resulted to effective outcomes and 19 patients out of 20 were able to go back to work [44].

Experimental cadaveric tests of the healthy spine demonstrated that the posterior elements only withstand 20% of the compressive loads and the rest (80%) passes through the vertebral body [45]. *In vitro* studies showed that the spinal loads in flexion-extension were transferred by almost the same and opposite loads (about 165 N) in the anterior disc and posterior instruments; unlike, in lateral bending, the majority of loads were carried by equal and opposite loads in posterior instruments (about 140 N) [46]. Based on the Wolff's law, a sufficient compression is required to stimulate the bone remodeling. Once the load balance between the anterior and posterior column is not properly restored, increased or decreased stress may result to osteophyte formation or bone resorption, respectively [47].

A posterior fixation is used to increase the stability of the fused segment by decreasing the mobility of the FSUs. It has been proven that the use of pedicle screw fixation greatly increases the rigidity of the spinal segment after fusion surgery. Using a solid posterior fixation allows to share the loads between the anterior and posterior columns. Semi-rigid fixation is a potential alternative [48] to share more loads with the anterior column in the range of physiological loads, and also promoting the solid fusion of the adjacent vertebrae. Cadaveric experimental tests and finite element analyses showed that the interbody cages augmented by posterior instrumentation reduced the ROM at the fused segment to lower than 1^0 while it was between 2^0 and 8^0 for uninstrumented (intact) model [11, 15, 49, 50].

The sufficient strength of the screw anchoring is required to fulfill the efficacy of the posterior fixation against the imposed loads. Pedicle screws with outer diameter of 6.5 mm vs. 4.5 mm increased the pullout strength from 0.97 ± 0.05 kN to 1.53 ± 0.01 kN [51]. Osteoporosis causes the compromised bone quality and may drastically reduce the pullout strength from more than 1000 N to below 400 N [52]. Double threaded pedicle screws are proposed to increase the pullout strength of single threaded one; the pullout strength in cycling loading condition was 140 ± 37.9 N for the former and was 121.8 ± 41 N for the latter (p=0.44) [53].

2.4.3 Failure modes in TLIF

A fusion rate of 92.5% to 97% is reported by the clinical follow-up studies after TLIF [5, 8, 54-56]. Clinical studies reported failures of the TLIF procedure, which is attributed to cage subsidence, failure of the posterior instrumentation, and adjacent segment degeneration (ASD). Cage

subsidence is a situation that endplate cannot tolerate an excessive amount of load imposed by the interbody cage resulting in the endplate collapse and loss of the fusion failure [57] (Figure 2-13). Several risk factors of cage subsidence in TLIF have been identified, such as the cage geometry (shapes, sizes, etc.) [5, 7-12], single cage vs. paired cages [13] , and the use of unilateral posterior fixation vs. bilateral one [14, 15]. Placement of expandable cages increased the segmental lordosis from 3.54° before surgery to 6.37° by 24 months with insignificant subsidence and fusion rate of 92.5% [58]. Placement of an interbody cage with a greater height offers a better restoration of segmental lordosis but requires a higher distraction. Increasing distraction of the segment ascends the compression force in endplate-cage interface that may results to a higher risk of cage subsidence. Experimental tests using cadavers showed that this compressive force was 8.8 N with the insertion of a 6 mm height cage while it increased to 21.5 N with a cage of 8 mm height [16]. 16% more anterior placement of the interbody cages resulted to 2.11° more segmental lordosis restoration [17] and a lower risk of cage subsidence due to shifting the endplate-cage interface to the peripheral region of the endplates with superior mechanical strength. Osteoporosis increased the risk of cage subsidence up to 8 times higher [59], thus enough contact between the interbody cages and endplates should be maintained to uniformly distribute the loads and avoid the cage subsidence [11].

The stiffness of the posterior fixation mostly depends on the diameter of rods, their material, and their diameter. It is reported that 40% elongation of the diameter of the rods increased the bending moment and axial force on the fixator up to 82% and 33% [60]. The risk of rod failure is higher in smaller rods due to the greater deformation and consequently higher internal stresses; however, more rigid rods apply higher portion of the loads to the pedicle screws increasing the risk of pullout. Some other aspects of pedicle screw fixation in terms of pullout strength are described in Figure 2-13.
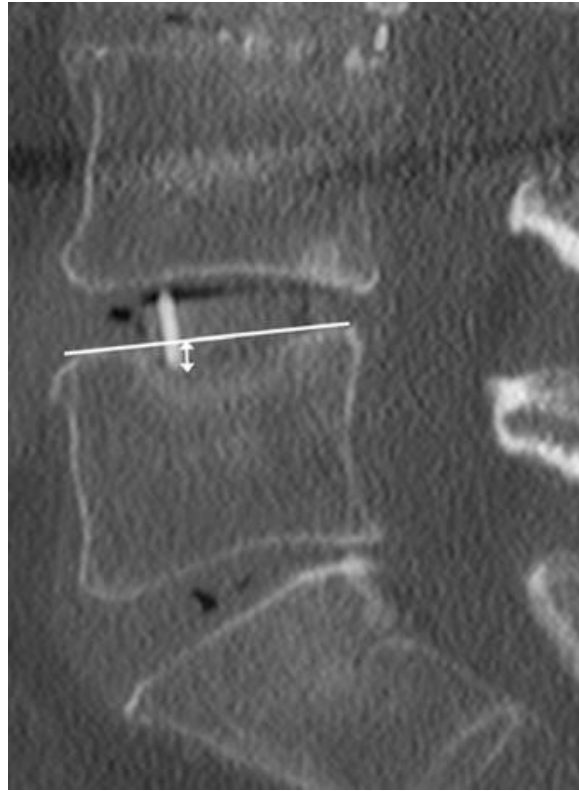
Figure 2-13 Measurement of the cage subsidence from the radiological evaluation (Image taken from [6])

Since TLIF restrains the mobility of the fused segment, the motion of the adjacent segments will increase to achieve the total required displacement resulting to the elevated intradiscal pressure in those FSUs [61, 62]. It is reported that the stresses in the intervertebral discs of the adjacent segments increased up to 10% when the lumbar spine underwent whether single or multi-level fusion, but the increment was higher in multi-level TLIF [62]. In addition to the stiffness of the fused segment, higher sagittal orientation of the facet joints at the adjacent segments surged the risk of symptomatic adjacent segment disease [61]. Nevertheless, the mechanical interventions are not the only risk factors of ASD. Physiological and environmental factors also contribute the initiation and progression of the disc degeneration.

2.5 FEM of the lumbar spine and TLIF

2.5.1 Finite element modeling of the spine

2.5.1.1 FEM of vertebrae

The geometrical parameters of the vertebrae such as their dimensions and morphology can be extracted from medical images. Two main approaches exist to develop a FEM of the spine: "generic" and "patient-specific". The generic geometry modeling is based on anatomical measurements integrated in a parametrized approach [63]. In certain models, the geometry is assumed as symmetric in the sagittal plane (Figure 2-14. A). Personalized models can be obtained through medical images converted into different mesh elements [63-65] (Figure 2-14. B). Isotropic [66-69] or transversely isotropic [70, 71], or orthotropic [72] elastic and elasto-plastic materials can be used to simulate the mechanical behavior of the bony components.

A   B
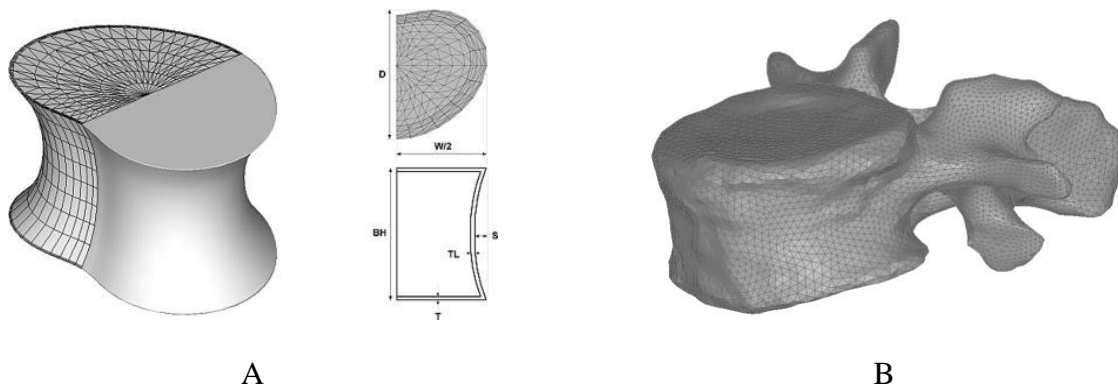
Figure 2-14 A) Generic model with parametrized body height, width, depth, and thickness [73], and B) a specimen FEM of the L3 lumbar vertebra

2.5.1.2 FEM of lumbosacral functional units or segments

The lumbosacral FEMs consist of lumbar vertebrae (L1 to L5), sacrum, IVDs, spinal ligaments, and pertinent joints. These models are used to study the spine biomechanics, better understand mechanisms of spinal injuries, and analyze the spinal instrumentation.

The IVD may be modeled as axisymmetric [74, 75] or symmetric [74, 76] volumetric elements. Some more realistic models consider the concave profiles of the caudal and cranial surfaces of the IVD in contact with the vertebral endplates [7, 14, 15, 77, 78]. 3D elements allow to simulate AF ground material and NP. Truss or bar elements in the 3D solid elements can represent the collagen fibers of the AF. The spinal ligaments may be included into the FEMs by using the cross-sectional area measured experimentally. The spinal ligaments may be modeled as 2-node truss, cable, or spring elements with linear or non-linear elastic or viscoelastic behaviour. The facet joints can be integrated in the model by using contact elements with initial gaps between 0.4 and 1.25 mm [67, 70, 77-79].

Incompressible hyperelastic Neo-Hookean or Mooney-Rivlin formulation can represent the mechanical behaviour of the NP and AF [66-71]. Linear or non-linear elastic or viscoelastic may mimic the mechanical behavior of collagen fibers. Linear elastic [71], piecewise non-linear [69], non-linear [66, 68, 70], or exponential [72] stress-strain curves may be used to represent the spinal ligaments behavior.

The volumetric (solid) elements in these models allow to accurately compute the stresses and strains in the spinal parts [80-82]. To shorten the processing time, when a detailed stress analysis is not necessary, vertebrae can be assumed as rigid bodies and other parts may be simulated as simplified elements [82]. The hybrid modeling (rigid and flexible elements) allows to calculate the stresses and strains in the target regions while the rest of components are simulated as rigid bodies [80, 82].

2.5.2 Critical review of lumbar spine finite element models

Several FEMs of the spine have been developed to study the stress distribution in different spinal components and to assess the posture of the lumbar spine under compression, lateral bending, and axial rotation. Shirazi-Adl [77] developed and validated a FEM of the L1-L5 lumbar spine based on CT images taken from cadaveric specimen and validated it by using the results of his previous experimental tests. Little et al. [69] developed a FEM to investigate the role of geometrical parameters of the spine on the coupled rotations. They used a 59-year old female cadaver to build the L1-L5 lumbar model and validated it against the *in-vivo* radiological measurements performed

by Pearcy [83]. In 2009, Zander et al. [68] developed a FEM of the L1-L5 lumbar spine based on CT measurements of cadavers and validated against the available experimental data. This model was used to evaluate the kinematics of the spinal motion segment with the use of a developed arthroplasty implant in flexion, extension, lateral bending, and axial rotation. Ayturk and Puttlitz [72] created a L1-L5 lumbar FEM on the basis of CT images of a 49-year old female, and validated it by using the ROM under a 7.5 Nm bending moment simulating flexion, extension, lateral bending, and axial rotation. Based on the CT scan of a cadaveric subject, Kiapour et al. [67] developed a FEM of the L3-S1 spine and validated it by comparing the ROM in physiological loading conditions with those experimentally measured on human cadavers. This model has been widely used to investigate different spinal fusion techniques as well as artificial disc replacement. To mimic muscle forces and upper limbs weight, a compressive 400 N follower load was applied before the segment underwent physiological loads [7]. In 2012, Schmidt et al. [70] built a FEM of the L1-L5 spine from CT-scan images of a 46-year old cadaveric subject and validated it against the experimental data of ROM. A 500 N preload was applied to simulate the upper body weight and local muscle loads, and then the biomechanics of the multilevel disc arthroplasty was assessed. A FEM of the L1-L5 spine was created by Li et al. [84] using the CT-scan images of a 19-year old healthy subject and was validated to assess the biomechanical performance of a new semi-flexible posterior fixation.

SM2S (Spine Model for Safety and Surgery) is a detailed and realistic model of the whole spine developed and validated within the iLab-Spine (partnership between the Laboratory of Applied Biomechanics of IFSTTAR/AMU, Polytechnique Montréal, École de technologie supérieure and other hospitals) [85]. The geometry is reconstructed on the basis of CT-scan images (0.6 mm slice thickness) of a 50th percentile healthy male, and includes all the vertebrae, pelvic, IVDs, spinal ligaments, and facet joints [78,79]. The cortical and trabecular bony parts are modeled by 4-node tetrahedral elements by considering the local variation of thickness of the cortical shell. The 8-node hexahedral elements represent the IVDs and 8 layers of collagen fibers (uniaxial springs) reinforce the AF. The spinal ligaments are modeled by the 4-node shell elements, except the CLs which were modeled by 3-node shell elements. Bony elements are governed by the homogenous elasto-plastic Johson-Cook law. The IVDs are assumed as the hyper-elastic Mooney-Rivlin formulation while the collagen fibers are governed by a non-linear load-displacement curve. The spinal ligaments

follow the generalized Maxwell-Kelvin-Voigt viscoelastic formulation. Facet joints are modeled by a frictionless contact interface.

These FEMs are associated with the inherent limitations, which are caused by the complex geometry of the spine, non-linear behavior of the tissues, complicated loading and boundary conditions, and variability of the reference specimens. The FEMs generally are validated against the available experimental data for the ROM in compression or pure moment, but intradiscal pressure and facet joint force might vary between the models [86], which weaken their robustness to predict different biomechanical measures of TLIF. Also, they are built based on the geometry of only a limited number of specimen, hence hindering the inter-variability between different spinal geometries. Not only the geometry, but material properties of the spinal elements change with different situation such as age, gender, and quality of life. Rarely, these FEMs were subjected to the combined loading condition which are more realistic and predictive. In brief, although these developed FEMs are capable to simulate some biomechanical aspects of the spine, a significant effort is still required to gain more realistic FEMs.

2.5.3 Critical review of previous biomechanical FEM studies of TLIF

Li et al. (2015) [84] developed a non-linear FEM of the L3-S1 to compare the biomechanics of pedicle screw-rod vs. plate as posterior fixation in TLIF. Also, this study investigated the difference of the unilateral vs. bilateral posterior fixation under a bending moment of 7.5 Nm following a 400 N follower load. The TLIF was done at the L4-L5 level, and the endplate-cage interface was modeled as a finite sliding contact with a friction coefficient of 0.2. The results demonstrated that both posterior instrumentations remarkably reduced the ROM to around 1°, and the plates had identical outcomes to the rods. Bilateral vs. unilateral posterior fixation was more effective to decrease the ROM (up to 74% with unilateral instrumentation and 88% with bilateral). The maximum Von-Mises stresses in caudal screws ranged from 0.9 to 2.2 times higher with the use of plates than rods.

Faizan et al. (2014) [7] used a previously validated FEM of the L3-S1 lumbar spine to assess the risk of cage subsidence in the TLIF as a function of cage footprint as well as to evaluate a new designed interbody cage under a combination of 10 Nm bending moment and 400 N follower load.

Unlike the other finite element models of TLIF that did not consider the distraction procedure, in this study, distraction procedure was modeled to assure an intimate endplate-cage contact (rough friction contact). The use of an interbody cage with 75% larger footprint (490 vs. 280 mm^2), although increasing the sustained compressive load at the endplate-cage interface by about 300%, it reduced the maximum stresses up to 50% resulting in a lower risk of cage subsidence

Tang (2015) [87] modified an existing FEM of the L3-L5 to compare the biomechanics of TLIF and PLIF. The degrees of freedom of the L5 inferior surface were fixed, and the model was subjected to a combination of 800 N compressive load and 10 Nm bending moment in different anatomical planes. The endplate-cage interface was virtually considered as a solid fusion. The result showed that TLIF and PLIF increased the intradiscal pressure at the level above the fusion up to 78.3% and 104.3%, respectively. To compensate the lack of mobility at the fused segment, the ROM was increased by 19.2% at the level above with potentially increasing risk of ASD.

Agrawal et al. (2013) [10] developed a L4-L5 FEM to relate the stress distribution at the endplate-cage interface to the conformity of a tissue-engineered polycaprolactone-hydroxyapatite (PCL-HA) interbody. The interface was modeled as a surface-to-surface finite contact with the friction coefficient of 0.3, and a 400 N follower load followed by a 7.5 Nm bending moment were applied to the FEM. Using the conformal vs. non-conformal interbody increased the contact area by 55% and 229% in flexion and extension, respectively. The increased contact area, subsequently, resulted to the reduced stresses at the endplate-cage interface by 33% and 38% in flexion and extension, respectively, thus a lower risk of cage subsidence is expected.

Lo et. al. (2011) [88] used a previously validated FEM of the L1-L5 lumbar spine and simulated TLIF at the L3-L4 motion segment with the use of two posterior instrumentation systems, namely Coflex-F and pedicle screw-rod. The endplate cage interface was modeled as a surface-to-surface contact with a friction coefficient of 0.8, which represents the fusion condition. The adapted FEM were subjected to a 400 N follower load followed by a 10 Nm bending moment representing physiological loadings in lateral bending and axial rotation. The Coflex-F vs. pedicle screw-rod posterior instrumentation increased the maximum stresses at the endplate-cage interface about 50%, 80%, and 50% in flexion, lateral bending, and axial rotation.
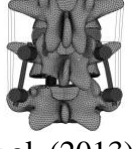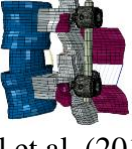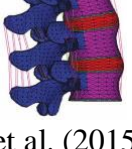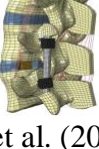
Chen et al. (2012) [15] adapted a L1-S1 lumbar FEM and simulated TLIF at the L4-L5 motion segment to evaluate the difference of unilateral and bilateral posterior fixation. A surface-to-surface

contact with friction coefficient of 0.8 mimicked the endplate-cage interface. A 10 Nm bending moment in physiological planes was applied to the FEM in presence of a 400 N follower load. The measured ROM at the fusion segment with unilateral posterior instrumentation increased up to 22%, 59%, and 32% in extension, lateral bending, and axial rotation, respectively, compared to the bilateral posterior fixation. The maximum stresses at the endplate-cage interface with unilateral posterior instrumentation also increased by 33%, 27%, and 45% in extension, lateral bending, and axial rotation, respectively.

Ambati et al. (2015) [14] modified a previously validated model of the L3-L5 lumbar spine to simulate TLIF at the L4-L5 motion segment with unilateral and bilateral posterior fixations. The endplate-cage contact was considered as a sliding algorithm with the friction coefficient of 0.2, and a 10 Nm bending moment was applied to simulate flexion, extension, lateral bending, and axial rotation. More than 50% of the ROM at the fused segment was remained with unilateral instrumentation, while it was less than 10% with bilateral one. The maximum stresses at the endplate-cage interface was up to 6 times higher with unilateral posterior fixation.

Xu et al. (2013) [13] performed a comparison study between the use of single- or paired-cage constructs in TLIF by using a FEM of L3-L5. Unlike the other studies, the endplates were removed at the fused segment. To avoid the slippage of the cage over endplates, a surface-to-surface contact with a friction coefficient of 0.8 was incorporated. The physiological loads were simulated as a combination of 400 N follower load over 7.5 Nm bending moment. The maximum stresses at the endplate-cage interface was almost 46% higher with single-cage compared to the paired one. The maximum stresses in the posterior screws also increased up to 75% with single-cage placement.

Table 2-1 Summary of the available finite element models have been used to investigate biomechanics of TLIF

Model	Description	Application
Lo et al. (2011) [88]	L1-L5 TLIF at L3-L4 Coefficient friction: 0.8 Follower load: 400 N Bending moment: 10 Nm	Compare Coflex-F posterior fixation with pedicle screw-rod system
Chen et al. (2012) [15]	L1-S1 TLIF at L4-L5 Coefficient friction: 0.8 Follower load: 400 N Bending moment: 10 Nm	Investigate biomechanical difference of unilateral vs. bilateral posterior fixation in terms of ROM.
Xu et al. (2013) [13]	L3-L5 TLIF at L4-L5 Coefficient friction: 0.8 Follower load: 400 N Bending moment: 7.5 Nm	Compare the risk of cage subsidence as function number of placed cages (Single- vs. paired-cage)
Agrawal et al. (2013) [10]	L4-L5 TLIF at L4-L5 Coefficient friction: 0.3 Follower load: 400 N Bending moment: 7.5 Nm	Compare the risk of cage subsidence in placement of the conformal vs. non-conformal tissue-engineered interbodies
Faizan et al. (2014) [7]	L3-S1 TLIF at L4-L5 Coefficient friction: 0.2 Follower load: 400 N Bending moment: 10 Nm	Assess the role of cage footprint in the risk of cage subsidence.
Tang et al. (2015) [87]	L3-L5 TLIF at L4-L5 Coefficient friction: Solid Follower load: 800 N Bending moment: 10 Nm	Compare the risk of adjacent segment degeneration in TLIF and PLIF.
Ambati et al. (2015) [14]	L3-L5 TLIF at L4-L5 Coefficient friction: 0.2 Follower load: 400 N Bending moment: None	Compare the stability of the fused segment with unilateral vs. bilateral posterior instrumentation.
Li et al (2015) [84]	L3-S1 TLIF at L4-L5 Coefficient friction: 0.2 Follower load: 400 N Bending moment: 7.5 Nm	Compare biomechanics of pedicle screw-rod with pedicle screw-plate posterior fixation.

The presented FEM models in Table 2-1 have been developed to investigate the biomechanical aspects and risk factors of cage subsidence in TLIF. Cage geometry (shapes and sizes), single cage vs. paired cages, type of the posterior instrumentation (pedicle screw-rod vs. Coflex-F implant), and the use of unilateral vs. bilateral posterior fixation are identified as the risk factors associated with the mechanical failures of TLIF. The clinical observations have shown that insertion of a thicker cage allows superior restoration of SLL, although it increases the risk of cage subsidence; anterior placement of the cage is clinically proven a lower risk of cage subsidence. These two parameters of TLIF procedure (Height of interbody cage and its placement strategy at intervertebral disc space) are not yet investigated through a biomechanical study to evaluate their influence in the risk of cage subsidence.

CHAPTER 3   RESEARCH RATIONALE AND OBJECTIVES

In summary, the preceding chapter allowed to critically review the TLIF as a surgical intervention to restore the intervertebral body height, the lumbar lordosis, as well as to serve postoperative stability to the lumbar spine so as to obtain a solid fusion. In TLIF, the anterior stability is achieved by means of one or more interbody cages through a unilateral approach while posterior instrumentation provides additional stability. Cage subsidence is a reported problem leading to the failure of the TLIF, which results in the loss of the restored lordosis angle and requires a revision surgery in some cases. The failure of the anterior column might also increase the risk of posterior instrumentation failure. The literature reports that a thicker cage offers a higher restoration of the lordosis angle as it increases the height of the anterior column. However, the insertion of a thicker cage necessitates a greater distraction of the anterior column; therefore, the compression forces at the endplates-cage interface increase the mechanical stresses on the endplates. Also, clinical observations have shown that anterior placement of the cage not only facilitate the segmental lordosis restoration, but also translates the maximum stress on a region of the endplates with superior mechanical strength.

Thus, the research question of this master research project is as follows:

> *How do the height of cage, the cage placement strategy, and bone quality biomechanically affect the segmental **lumbar lordosis** and risk of cage **subsidence** early postoperatively?*

The general objective of this project is to numerically assess the segmental lumbar lordosis increment and risk of cage subsidence as a function of cage height, placement strategy and bone quality.

To address the general objective, two specific objectives were defined:

Objective 1: To develop and validate a detailed finite element model (FEM) of TLIF, which involves all the elements of a L4-L5 functional unit and different aspects of instrumentation corresponding to the standard procedure of TLIF.

Objective 2: To investigate the change in achieving segmental lumbar lordosis after cage placement and the risk of cage subsidence under physiological loading conditions (flexion, extension, lateral bending, and axial rotation) based on the cage height, its placement strategy, and bone quality.

To address the research question and to perform the objectives above, the workflow presented in Figure 3.1 is proposed. The geometry of the L4-L5 segment, including the cortical and trabecular bones, IVD, seven spinal ligaments, and facet joints, will be extracted from SM2S model. The material properties will be adapted from the literature. This FEM will be used to simulate different steps of TLIF such as intervertebral disc space preparation, cage insertion with different heights and placement strategy, and posterior instrumentation. A verification and validation (V&V) study will be performed to establish the model credibility. In the modeling process, the achieved SLL after the cage placement will be calculated before performing the posterior fixation. To compare the risk of cage subsidence among the different configurations, the stress distribution at the endplate-cage interface in the physiological loading conditions will be calculated.
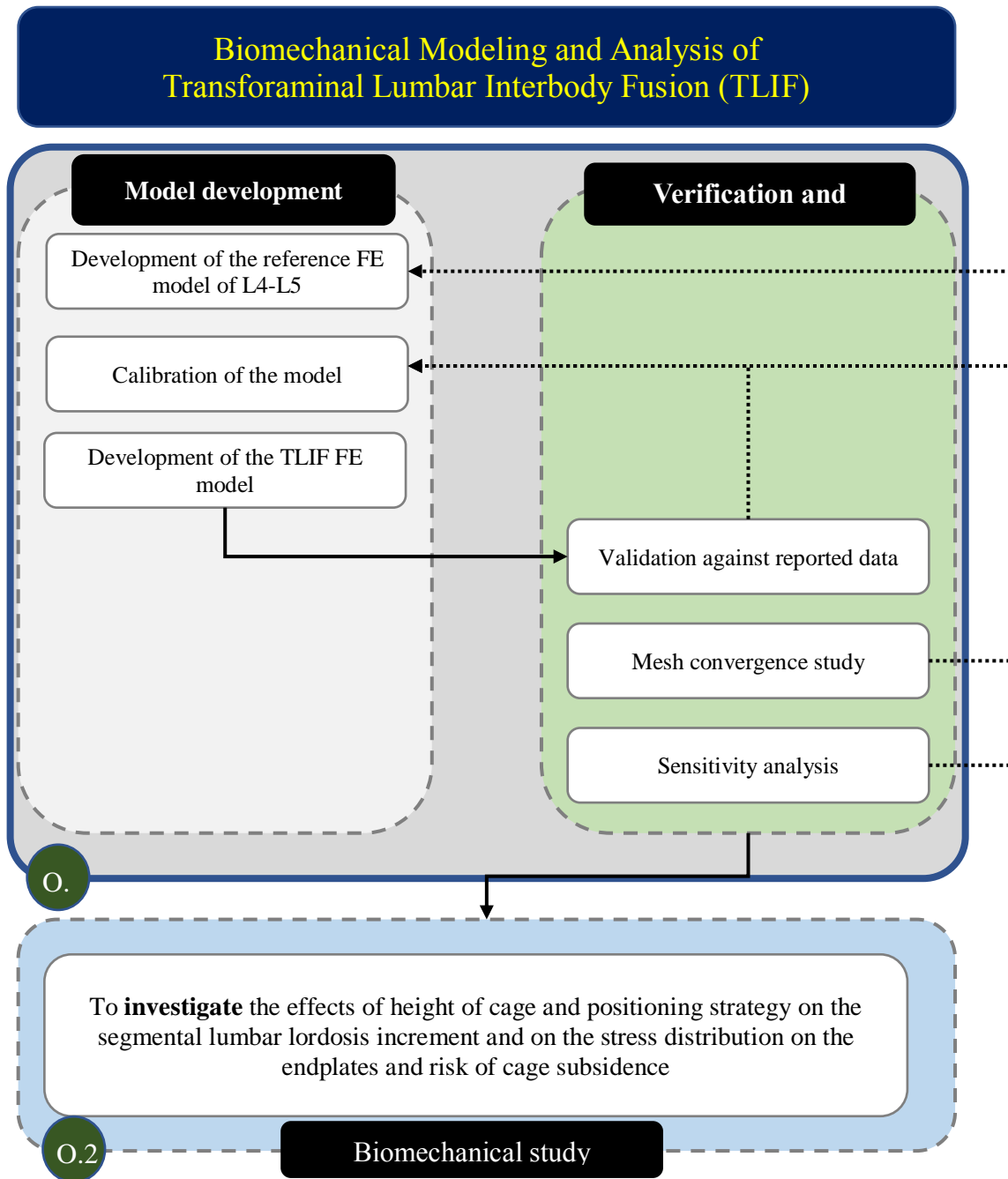
Figure 3-1 Schematic workflow of this project to address the research question

CHAPTER 4   ARTICLE I: BIOMECHANICAL ANALYSIS OF SEGMENTAL LUMBAR LORDOSIS AND RISK OF CAGE SUBSIDENCE WITH DIFFERENT CAGE HEIGHTS AND ALTERNATIVE PLACEMENTS IN TRANSFORAMINAL LUMBAR INTERBODY FUSION

4.1 Presentation of the manuscript

The main realization of the objectives of this master thesis is presented in the manuscript entitled *"Biomechanical analysis of segmental lumbar lordosis and risk of cage subsidence with different cage heights and alternative placements in transforaminal lumbar interbody fusion"*, for which the contribution of the first author is considered to be 80%. This manuscript was submitted to the journal of *Medical & Biological Engineering & Computing* on April 9th, 2019.

4.2 Scientific manuscript: Biomechanical analysis of segmental lumbar lordosis and risk of cage subsidence with different cage heights and alternative placements in transforaminal lumbar interbody fusion

Sajjad Rastegar [a,b,c], Pierre-Jean Arnoux Ph.D. [c,d], Xiaoyu Wang Ph.D. [a,b,c], Carl-Éric Aubin Ph.D., P.Eng. [a,b,c]

(a) Department of Mechanical Engineering, Polytechnique Montréal, P.O. Box 6079, Downtown Station, Montreal (Quebec), Canada H3C 3A7

(b) Sainte-Justine University Hospital Center, 3175, Cote Sainte-Catherine Road, Montreal (Quebec), Canada H3T 1C5

(c) iLab Spine – International Laboratory – Spine Imaging and Biomechanics, Canada/France

(d) Laboratoire de Biomécanique Appliquée, UMRT24 IFSTTAR/Aix-Marseille Université, Boulevard Pierre Dramard, 13916 Marseille Cedex 20, France

Keywords

Finite Element Analysis, TLIF (Transforaminal lumbar interbody fusion), Cage Subsidence, Interbody cage, Biomechanics, Spine

4.2.1 Abstract

OBJECTIVE: Transforaminal lumbar interbody fusion (TLIF) is a surgical procedure involving the introduction of an interbody cage to restore the intervertebral body space, achieve anterior fusion in addition to posterior fusion with a rigid lumbar segmental fixation. Cage subsidence due to stresses at the contact between the cage and the vertebra is one of the concerns. The objective was to numerically assess the biomechanics of TLIF in terms of the resulting segmental lordosis (SLL) and stresses at the bone-implant interface as functions of different TLIF parameters.

METHODS: A previously validated finite element model of the lumbar spine was adapted to numerically simulate the biomechanics of the TLIF at L4-L5 such as partial removal of intervertebral disc and tissues, intervertebral distraction, cage insertion, and posterior fixation with pedicle screws and 4.5 mm titanium rods. The tested instrumentation parameters were the cage height (8 vs. 10 mm) and cage placement (oblique asymmetric, vs. anterior symmetric). The effects of bone quality (normal vs. osteoporotic) were also evaluated. A total of 8 TLIF scenarios were simulated. Functional loadings of 10 Nm were simulated respectively in flexion, extension, lateral bending, and transverse plane torsion after the application of a follower load of 400 N.

RESULTS: The SLL was increased by 0.9° (11%) and 1.0° (13 %), respectively in oblique asymmetric and anterior symmetric cage placement with 8-mm height; they were 1.4° (18%) and 1.7° (21 %) when simulating with the cage of 10-mm height. The change in the range of motion after the simulated posterior fixation was lower than 1° in all the simulated TLIF scenarios. Compared to the 8-mm cage, maximum stresses at the cage-bone interface with the 10-mm cage were up to 16% higher in simulations with both normal and osteoporotic bone models. Maximum

stresses in oblique asymmetric cage placement were respectively up to 41% and 43% higher than the anterior symmetric placement in normal and osteoporotic bone models, respectively.

CONCLUSION: The simulated SLL with the 10-mm cage were higher than those with 8-mm cage. The resulting SSL with the oblique asymmetric placement was very close to that with anterior symmetric placement. The maximum stresses at the bone-cage interface with oblique asymmetric placement were higher than the symmetric placement; greater cage height also resulted in higher maximum stresses, which may increase the risk of cage subsidence. Although the osteoporotic bone had almost identical maximum stresses to normal bone, the risk of cage subsidence should be higher due to its lower mechanical strength.

4.2.2 Introduction

Transforaminal lumbar interbody fusion (TLIF) is a surgical procedure to restore the intervertebral body height, the lumbar lordosis (LL) and stability, and to achieve and maintain the global sagittal balance. This involves the removal of the nucleus pulposus and a portion of the annulus fibrosus, followed by decompression of the segment and the placement of an interbody cage through a unilateral approach. This is aimed at achieving an anterior interbody fusion in addition to the posterior one by a solid segmental fixation [2,15]. There exist different cages in terms of shape (bullet shape, kidney (moon)-shape, and articulating semilunar) with a wide variety of geometries (height or thickness, width, footprint) having flat or biconvex faces in contact with the endplates.

One of the mechanical complications of the TLIF surgical intervention is cage subsidence, a situation where a cage enters into the vertebral body and consequently results in the loss of intervertebral body height and segmental lumbar lordosis (SLL) created intraoperatively by the instrumentation. The reported incidence of TLIF subsidence is between 8.6% and 38.1% [22,24,26]. Several risk factors of cage subsidence in TLIF have been identified, such as the cage geometry (shapes and sizes) [1,7,9,12,20-22], single cage vs. paired cages [35], and the use of unilateral posterior fixation vs. bilateral one [3,6].

Biomechanical analysis using finite element models showed that articulating vertebral interbody (AVID) cage allowed larger cage footprint than the traditional bullet-shape cage (e.g., 490 vs. 280

mm2) to bear about 300% more functional load and reduced the maximum stresses by about 50%, resulting in a lower risk of cage subsidence [12]. Biconvex shapes were shown to allow better cage fitting, but with loads more concentrated in the medial region of the endplates with relatively lower mechanical strength than peripheral cortical bone, thus higher risk of cage subsidence [7]. Using paired- vs. single-cage configurations resulted in 55.2% lower stress at the bone-cage interface (49.77 vs. 77.23 MPa) and subsequently lower risk of cage subsidence [35].

A thicker cage is generally more effective for SLL restoration, but requires more intervertebral distraction for its placement, which increases the risk of cage subsidence due to the higher compressive forces at the bone-cage interface (8.8 N with 6-mm cage vs. 21.5 N with 8-mm cage in a biomechanical experiments using cadaveric lumbar spines) [22,32]. Clinical studies showed that a kidney-shape cage placed 16% more anteriorly vs. a medial placement of a bullet-shape cage, resulted in an SSL increase of 2.11^0 [21] and reduced the risk of cage subsidence by shifting the bone-cage contact more to the peripheral region of the endplates with superior mechanical strength. Wedged cages (vs. flat or parallel cages) are reported to allow better lordosis restoration; increasing the wedge angle from 4° to 15°, and increased the resulting SLL from 2.6° to 6.5° [18].

Clinical studies, experiments using cadaveric spines, and numerical analyses have been done on the use of interbody cages of different shapes, configurations, and heights. However, the effects of essential cage parameters are not yet fully understood; therefore, systematic biomechanical investigations remain to be performed to acquire comprehensive biomechanical facts to help understand and reduce the risk of cage subsidence. The objective of this study was to numerically assess the biomechanics of TLIF in terms of the resulting SLL and stresses at the bone-cage interface as functions of the cage height, its placement strategy, and the bone quality.

4.2.3 Methods and materials

4.2.3.1   Finite element model of the L4-L5 segment

A detailed finite element model (FEM) of L4-L5 functional spinal unit was created based on a previously developed and validated FEM of the spine [10,11] (Figure 4-1). The FEM was adapted and refined to simulate the biomechanics of the TLIF, including intervertebral space preparation, cage insertion, and posterior fixation [2,15]. The geometric model of the spine was reconstructed

using medical images acquired through a CT-scan (0.6 mm slice thickness) of a 50th percentile healthy man [10,11]. The model consisted of the vertebral body (cancellous and cortical bones), the posterior arches, the intervertebral disc, the facet joints, and seven ligaments, i.e. the anterior longitudinal ligament (ALL), the posterior longitudinal ligament (PLL), the ligamentum flavum (LF), the capsular ligaments (CL), the intertransverse ligament (ITL), the interspinous ligament (ISL), and the supraspinous ligament (SSL) (Figure 4-1).

Each vertebra was meshed with 4-node solid elements, representing the trabecular bone enveloped by a layer of cortical bone whose thickness varied in five regions: vertebral endplates and anterior walls of the vertebral body (0.4 mm), upper pedicle (2 mm), lower pedicle (1.87 mm), posterior processes (1 mm), and insertion area of pedicle screws (0.8 mm) [4,17,30] (Figure 4-2). The annulus fibrosus was modeled with five concentric layers of 8-node solid elements between the two vertebrae, reinforced by spring elements to simulate the collagen fibers oriented at $\pm35°$. The nucleus pulposus was meshed with 8-node elements. All ligaments were meshed with 4-node shell elements, except the CL, which was represented by 3-node shell elements. To balance the computation cost and analysis accuracy for this study, we performed a mesh convergence study to determine adequate element sizes (Figure 4-1 and Figure 4-2).

Non-linear material properties were implemented to model the mechanical behavior of the spinal elements in physiological loading conditions. The cortical and trabecular bones were modeled as homogenous isotropic materials governed by the elastoplastic Johnson-Cook constitutive law [34] The nucleus pulposus and annulus fibrosus were modeled as Mooney-Rivlin hyperelastic material while collagen fibers were incorporated as one-dimensional (1D) spring elements acting in tension only. The non-linear behavior of the spinal ligaments was modeled with a generalized Maxwell-Kelvin-Voigt constitutive law, and the failure criteria was incorporated based on the maximum tensile strain level [34]. The material properties of the elements were initially defined using numerical results from the literature (Tables 1, 2, and 3). Material properties of osteoporotic bone were modeled by reducing Young's modulus of cortical (33%) and trabecular bone (66%) [28]. To model the zygapophyseal facet joints, a general purpose contact was used with an initial gap of 0.5 mm [12] and Coulomb friction coefficient of 0.2 [25] between the two facets of the articulation. Tied contacts were modeled between the ligaments and the cortical bone at their attachment sites. The mechanical properties of the aforementioned modeling elements were adjusted and calibrated

such that the load-displacement results of functional loading simulations corresponded to results from experiments on cadaveric lumbar spines [8,16,19].

4.2.3.2   Simulation of TLIF procedure

The surgical procedure of TLIF was modeled and simulated using the FEM of the L4-L5 functional spinal unit. The partial discectomy through the unilateral approach was modeled by removing the elements corresponding to the posterior-left portion of the annulus fibrosus and nucleus pulposus. A facetectomy was simulated by removing the elements corresponding to the zygapophyseal joint to virtually make a window for the cage insertion (Figure 4-3.a). Four pedicle screws (40 mm long, 6.5 mm diameter; CD HORIZON® LEGACY^{TM}, Medtronic, Memphis TN) were modeled as rigid bodies, and their external surfaces were meshed with triangular shell elements. They were aligned with their corresponding vertebra based on a typical lumbar pedicle screw insertion technique [1,4]. Boolean operations between the screw and the vertebral models were performed to remove the cortical layer and trabecular core model elements to simulate screw insertion [4]. A point-to-surface contact with a Columb friction of 0.2 was modeled to represent the bone-screw interface.

The interbody cage models were based on a generic cage (CAPSTONE® interbody cage, Metronic, Memphis TN). The length and width of the models were 26 mm and 10 mm, respectively. Two cage heights were tested, i.e. 8 and 10 mm. For each model, we tested the oblique asymmetric and anterior symmetric placements, a total of four interbody cage scenarios (Figure 4-4). The cages were meshed with 4-node tetrahedral elements of 1.0 mm, and material properties of polyether ether ketone (PEEK) were assigned (E=3.4 GPa and v=0.4 [12]). The modeling of the cage insertion was based on the documented surgical technique [1]. First, the cage model was aligned to the superior endplate of L5, and a node-to-surface contact with a minimum distance of 0.5 mm and Columb friction coefficient of 0.2 was applied to the interface. Then, a distractive force was applied between L4 and L5 such that the intervertebral body space increased and there was no interference between the cage model geometry and the endplate geometries. Finally, the loads were released after node-to-surface contact was modeled between the cage and the adjoining endplates of L4 and L5 (Figure 4-3.b). The SSL was assessed before and after the simulation of the cage placement. This was done by measuring the angle between the superior endplate of L4 and inferior endplate of L5 [18]. After the simulation of the cage insertion, two

titanium rod (4.5 mm) models were aligned with screw head saddles and tied contacts were modeled between them to simulate the posterior fixation (Figure 4-3.c). The rods were meshed with 4-node tetrahedral solid elements of 0.5 mm characteristic length, and the material properties of Titanium alloy were adapted from literature (E=115 GPa and v=0.34 [12]).

The resulting FEM from the simulations of the cage insertion and posterior fixation was used to simulate physiological loading. The body weight was modeled as a 400 N follower load to the superior elements of L4 with the inferior endplate of L5 fixed in space. A 10-Nm functional load was simulated in the three anatomical planes, respectively, to simulate flexion (Fe), extension (Ex), right lateral bending (RLB), left lateral bending (LLB), right axial rotation (RAR), and left axial rotation (LAR). The ROM and maximum Von-Mises stresses were computed as a measure of the risk of cage subsidence.

All the simulations were performed using the RADIOSS v14.0 finite element package (Altair Engineering inc., Troy, USA) in a quasi-static condition using kinetic relaxation, a process enabling to lessen the effect of kinetic energy by setting the nodal velocity to zero [4].

4.2.4 Results

With the simulated normal bone quality, the anterior symmetric and oblique asymmetric placement of the cages increased the SLL by 0.9° and 1.0°, respectively, for the 8-mm height cage, and by 1.4° and 1.7° for the 10-mm one. SLL restorations with simulated osteoporosis were within 1.2% to those with the normal bone quality. With normal bone quality, the simulated ROMs of the FSU after the TLIF procedure were lower than 1° in all loading directions, while they ranged from 2° to 8°with the FSU without instrumentation. With simulated osteoporosis, the ROMs were slightly (about 8%) higher than those with normal bone quality. Oblique asymmetric vs. anterior symmetric placement increased the ROM of the instrumented FSU by 66% and 72% for the simulated normal and osteoporotic bone, respectively. Insertion of the 8-mm cage vs. the 10-mm one increased the ROM of the instrumented segment up to 43% and 48% in simulated normal and osteoporotic bone models, respectively.

For the 8-mm cage with normal bone quality, the maximum stresses at the bone-cage interface ranged from 82.1 to 98.4 MPa (anterior symmetric placement) and from 117.9 to 155.5 MPa

(oblique asymmetric placement) (Figure 4-5.a). For the 10-mm cage, they were from 88.2 to 107.2 MPa (anterior symmetric placement) and between 134.4 and 176.4 MPa (oblique asymmetric placement) (Figure 4-5.a). With osteoporosis bone, stresses at the bone-cage interface were about 2.5% lower (Figure 4-5.b). Oblique asymmetric as compared to the anterior symmetric cage placement increased the maximum stresses by up to 41% and 43% for the simulated normal and osteoporotic bone, respectively. Insertion of the 10-mm cage vs. the 8-mm one increased the maximum stresses by up to 16% in simulated normal and osteoporotic bone models.

For the 8-mm cage with normal bone quality, the maximum stresses in the posterior rods were between 128.9 and 230.3 MPa (anterior symmetric placement) and between 114.9 and 326.6 MPa (oblique asymmetric placement) (Figure 4-6.a). For the 10-mm cage, they ranged from 60.3 to 218.0 MPa (anterior symmetric placement) and from 69.6 to 262.5 MPa (oblique asymmetric placement) (Figure 4-6.a). With osteoporosis bone, stresses in the posterior rods increased up to about 120% (Figure 4-6.b). Oblique asymmetric vs. anterior symmetric placement increased the maximum stresses by up to 55% and 48% for the simulated normal and osteoporotic bone, respectively. In simulations with oblique asymmetric cage placement, stresses in the rod on the opposite side of the cage were higher than the other rod. Insertion of the 8-mm cage vs. the 10-mm one increased the maximum stresses up to 59% and 54% in simulated normal and osteoporotic bone models, respectively.

4.2.5 Discussion

A larger SLL restoration was observed in the simulations with a 10-mm cage compared to the 8-mm cage. This was expected from a geometric point of view because greater cage height means greater anterior intervertebral distance, thus higher SLL. Consequently, stresses at the bone-cage interface in simulations of 10-mm cage were always higher than the 8-mm cage. Cages of greater height required more intervertebral distraction for its proper placement, which initiated a higher compression force at the bone-cage interface generated by the tightening of the soft tissues, which translated in higher structural stiffness and lower ROM due to the nonlinear mechanical behavior of the intervertebral ligaments. This could explain why the maximum stresses in the rods with the 10-mm cage were lower than the 8-mm cage. In terms of stresses generated by the compression

forces as a function of cage height, the simulation results agreed with the reported experiments with cadaveric lumbar spines [3,32].

The simulated SLL restoration with the anterior symmetric cage placement was very close to that with the oblique asymmetric placement, but the maximum stresses at the bone-cage interface with anterior symmetric cage placement were consistently lower than those with oblique asymmetric placement. This may be explained by the fact that the resultant force at the bone-cage interface with anterior symmetric placement has a longer lever arm with respect to the posterior fixation, providing a mechanical advantage to balance the external loads. In this standpoint, with the use of similar interbody cage footprints and in the presence of a smaller compression force at the bone-cage interface, lower stress is expected with the anterior cage placement. Compared with oblique asymmetrical cage placement, the anterior symmetrically placed cage had more bone-cage contact area in the anterior part of the intervertebral body space (Figure 4-4) where the endplates have superior mechanical strength [12,33]. With the oblique asymmetric placement, reaction forces from the rods had, therefore, shorter lever arms with respect to the cage center − fulcrum point between the upper and lower vertebral bodies, resulting in a higher stress in the rods to balance the functional loads.

There was no difference in SLL restoration between normal and osteoporosis bones. Although the maximum stresses at the bone-cage interface for the simulated osteoporotic bone were very close to those of modeled normal bone, the risk of cage subsidence should be higher because the osteoporosis bones also have lower mechanical strengths due to decreased bone mineral density [5], as reported in clinical studies that showed that the risk of cage subsidence in osteoporosis spines was about 3 times higher than the risk in spines with normal bone quality [27,13]. The simulated osteoporosis bones had lower stiffness and provided less support of the functional loads as compared to the normal bones, making the rods subjected to higher loads and stresses.

Some simplifications and approximations were made in the modeling and simulations in this study (i.e. the cortical and trabecular bones were modeled as homogenous isotropic materials, the geometry and mechanical properties of the FSU were based on a generic 50th model, and screw insertion was model as a geometric Boolean operation between the screw and the vertebral models and with a contact definition between the two). These modeling simplifications and approximations are considered to have limited effects on the conclusions because this study

focused on the relative effects of the cage height, cage placement and bone quality which are common in TLIF for most of the cases. The modeling procedure could be further adapted for multi-level TLIF to assess the SLL restoration and risk of cage subsidence numerically. Also, this FEM can be used to examine the performance of any other interbody cages in TLIF aiming to achieve a higher SLL restoration with a lower risk of fusion failure.

4.2.6 Conclusion

A detailed FEM was developed to simulate the biomechanics of the TLIF procedure. The FEM allowed the assessment of the effects of the cage height, cage placement, and the bone quality on the SLL restoration and the risk of the cage subsidence. It was found that 10- vs 8-mm cage height resulted in up to 0.7° higher SLL restoration and 16% higher stresses at the bone-cage interface. Oblique asymmetric placement vs. anterior symmetric placement had almost similar SLL restoration, but the stresses at the bone-cage interface were up to 43% higher. Bone quality did not affect the achieved SLL; a higher risk of cage subsidence is expected for the osteoporotic spines although the maximum stresses at the bone-cage interface were 2.5% lower. The FEM presented in this study was shown to be a relevant tool to assess the biomechanics of TLIF. It could be further adapted to further assess the biomechanics of any interbody cage design, as well as to evaluate reported clinical findings towards the improvement of the TLIF procedure.

4.2.7 Acknowledgement

4.2.8 References

1. Agarwal A, Palepu V, Agarwal AK, Goel VK, Yildirim ED (2013) Biomechanical evaluation of an endplate-conformed polycaprolactone-hydroxyapatite intervertebral fusion graft and its comparison with a typical nonconformed cortical graft. Journal of biomechanical engineering 135:61005-61009. doi:10.1115/1.4023988

2. Agrawal BM, Resnick D (2012) Transforaminal Lumbar Interbody Fusion. In: Schmidek and Sweet Operative Neurosurgical Techniques. W.B. Saunders, Philadelphia, pp 1951-1954

3. Ambati DV, Wright EK, Jr., Lehman RA, Jr., Kang DG, Wagner SC, Dmitriev AE (2015) Bilateral pedicle screw fixation provides superior biomechanical stability in transforaminal lumbar interbody fusion: a finite element study. The spine journal 15:1812-1822. doi:10.1016/j.spinee.2014.06.015

4. Bianco RJ, Arnoux PJ, Wagnac E, Mac-Thiong JM, Aubin CE (2017) Minimizing Pedicle Screw Pullout Risks: A Detailed Biomechanical Analysis of Screw Design and Placement. Clinical Spine Surgery 30:E226-E232. doi:10.1097/BSD.0000000000000151

5. Bono CM, Einhorn TA (2003) Overview of osteoporosis: pathophysiology and determinants of bone strength. European spine journal, 12 Suppl 2:S90-S96. doi:10.1007/s00586-003-0603-2

6. Chen SH, Lin SC, Tsai WC, Wang CW, Chao SH (2012) Biomechanical comparison of unilateral and bilateral pedicle screws fixation for transforaminal lumbar interbody fusion after decompressive surgery--a finite element analysis. BMC musculoskeletal disorders 13:72. doi:10.1186/1471-2474-13-72

7. Cho W, Wu C, Mehbod AA, Transfeldt EE (2008) Comparison of cage designs for transforaminal lumbar interbody fusion: a biomechanical study. Clinical Biomechanics 23:979-985. doi:10.1016/j.clinbiomech.2008.02.008

8. Dahl MC, Ellingson AM, Mehta HP, Huelman JH, Nuckley DJ (2013) The biomechanics of a multilevel lumbar spine hybrid using nucleus replacement in conjunction with fusion. The spine journal 13:175-183. doi:10.1016/j.spinee.2012.11.045

9. Deng QX, Ou YS, Zhu Y, Zhao ZH, Liu B, Huang Q, Du X, Jiang DM (2016) Clinical outcomes of two types of cages used in transforaminal lumbar interbody fusion for the treatment of degenerative lumbar diseases: n-HA/PA66 cages versus PEEK cages. Journal of materials science Materials in medicine 27:102. doi:10.1007/s10856-016-5712-7

10. El-Rich M, Arnoux PJ, Wagnac E, Brunet C, Aubin CE (2009) Finite element investigation of the loading rate effect on the spinal load-sharing changes under impact conditions. Journal of biomechanics 42:1252-1262. doi:10.1016/j.jbiomech.2009.03.036

11. El-Rich M, Wagnac E, Arnoux PJ, Aubin CE (2008) Detailed modeling of the lumbar spine for trauma applications: preliminary results. Comput Method Biomec 11:93-94. doi:10.1080/10255840802297226

12. Faizan A, Kiapour A, Kiapour AM, Goel VK (2014) Biomechanical analysis of various footprints of transforaminal lumbar interbody fusion devices. Journal of spinal disorders & techniques 27:E118-127. doi:10.1097/BSD.0b013e3182a11478

13. Formby PM, Kang DG, Helgeson MD, Wagner SC (2016) Clinical and Radiographic Outcomes of Transforaminal Lumbar Interbody Fusion in Patients with Osteoporosis. Global spine journal 6:660-664. doi:10.1055/s-0036-1578804

14. Garo A, Arnoux PJ, Wagnac E, Aubin CE (2011) Calibration of the mechanical properties in a finite element model of a lumbar vertebra under dynamic compression up to failure. Medical & biological engineering & computing 49:1371-1379. doi:10.1007/s11517-011-0826-z

15. Gum JL, Reddy D, Glassman S (2016) Transforaminal Lumbar Interbody Fusion (TLIF). JBJS Essential Surgical Techniques 6:e22. doi:10.2106/JBJS.ST.15.00003

16. Heuer F, Schmidt H, Klezl Z, Claes L, Wilke HJ (2007) Stepwise reduction of functional spinal structures increase range of motion and change lordosis angle. Journal of biomechanics 40:271-280. doi:10.1016/j.jbiomech.2006.01.007

17. Hirano T, Hasegawa K, Takahashi HE, Uchiyama S, Hara T, Washio T, Sugiura T, Yokaichiya M, Ikeda M (1997) Structural characteristics of the pedicle and its role in screw stability. Spine 22:2504-2509; discussion 2510

18. Hong TH, Cho KJ, Kim YT, Park JW, Seo BH, Kim NC (2017) Does Lordotic Angle of Cage Determine Lumbar Lordosis in Lumbar Interbody Fusion? Spine 42:E775-E780. doi:10.1097/BRS.0000000000001957

19. Jaramillo HE, Puttlitz CM, McGilvray K, Garcia JJ (2016) Characterization of the L4-L5-S1 motion segment using the stepwise reduction method. Journal of biomechanics 49:1248-1254. doi:10.1016/j.jbiomech.2016.02.050

20. Kim CW, Doerr TM, Luna IY, Joshua G, Shen SR, Fu X, Wu AM (2016) Minimally Invasive Transforaminal Lumbar Interbody Fusion Using Expandable Technology: A Clinical and Radiographic Analysis of 50 Patients. World neurosurgery 90:228-235. doi:10.1016/j.wneu.2016.02.075

21. Kim JT, Shin MH, Lee HJ, Choi DY (2015) Restoration of lumbopelvic sagittal alignment and its maintenance following transforaminal lumbar interbody fusion (TLIF): comparison between straight type versus curvilinear type cage. Eur Spine J 24:2588-2596. doi:10.1007/s00586-015-3899-9

22. Le TV, Baaj AA, Dakwar E, Burkett CJ, Murray G, Smith DA, Uribe JS (2012) Subsidence of polyetheretherketone intervertebral cages in minimally invasive lateral retroperitoneal transpsoas lumbar interbody fusion. Spine 37:1268-1273. doi:10.1097/BRS.0b013e3182458b2f

23. Lee CK, Kim YE, Lee CS, Hong YM, Jung JM, Goel VK (2000) Impact response of the intervertebral disc in a finite-element model. Spine 25:2431-2439

24. Lee N, Kim KN, Yi S, Ha Y, Shin DA, Yoon DH, Kim KS (2017) Comparison of Outcomes of Anterior, Posterior, and Transforaminal Lumbar Interbody Fusion Surgery at a Single

Lumbar Level with Degenerative Spinal Disease. World neurosurgery 101:216-226. doi:10.1016/j.wneu.2017.01.114

25. Li J, Shang J, Zhou Y, Li C, Liu H (2015) Finite Element Analysis of a New Pedicle Screw-Plate System for Minimally Invasive Transforaminal Lumbar Interbody Fusion. PloS one 10:e0144637. doi:10.1371/journal.pone.0144637

26. Malham GM, Parker RM, Blecher CM, Seex KA (2015) Assessment and classification of subsidence after lateral interbody fusion using serial computed tomography. Journal of Neurosurgery Spine 23:589-597. doi:10.3171/2015.1.SPINE14566

27. Oh KW, Lee JH, Lee JH, Lee DY, Shim HJ (2017) The Correlation Between Cage Subsidence, Bone Mineral Density, and Clinical Results in Posterior Lumbar Interbody Fusion. Clinical Spine Surgery 30:E683-E689. doi:10.1097/BSD.0000000000000315

28. Salvatore G, Berton A, Giambini H, Ciuffreda M, Florio P, Longo UG, Denaro V, Thoreson A, An KN (2018) Biomechanical effects of metastasis in the osteoporotic lumbar spine: A Finite Element Analysis. BMC musculoskeletal disorders 19:38. doi:10.1186/s12891-018-1953-6

29. Schmidt H, Kettler A, Heuer F, Simon U, Claes L, Wilke HJ (2007) Intradiscal pressure, shear strain, and fiber strain in the intervertebral disc under combined loading. Spine 32:748-755. doi:10.1097/01.brs.0000259059.90430.c2

30. Silva MJ, Wang C, Keaveny TM, Hayes WC (1994) Direct and computed tomography thickness measurements of the human, lumbar vertebral shell and endplate. Bone 15:409-414

31. Tome-Bermejo F, Pinera AR, Alvarez-Galovich L (2017) Osteoporosis and the Management of Spinal Degenerative Disease (I). The archives of bone and joint surgery 5:272-282

32. Truumees E, Demetropoulos CK, Yang KH, Herkowitz HN (2008) Effects of disc height and distractive forces on graft compression in an anterior cervical corpectomy model. Spine 33:1438-1441. doi:10.1097/BRS.0b013e318175c315

33. Tsitsopoulos PP, Serhan H, Voronov LI, Carandang G, Havey RM, Ghanayem AJ, Patwardhan AG (2012) Would an anatomically shaped lumbar interbody cage provide better stability? An in vitro cadaveric biomechanical evaluation. Journal of spinal disorders & techniques 25:E240-244. doi:10.1097/BSD.0b013e31824c820c

34. Wagnac E, Arnoux PJ, Garo A, Aubin CE (2012) Finite element analysis of the influence of loading rate on a model of the full lumbar spine under dynamic loading conditions. Medical & biological engineering & computing 50:903-915. doi:10.1007/s11517-012-0908-6

35. Xu H, Ju W, Xu N, Zhang X, Zhu X, Zhu L, Qian X, Wen F, Wu W, Jiang F (2013) Biomechanical comparison of transforaminal lumbar interbody fusion with 1 or 2 cages by finite-element analysis. Neurosurgery 73:198-205. doi:10.1227/01.neu.0000430320.39870.f7

36. Yang KH, Zhu F, Luan F, Zhao L, Begeman PC (1998) Development of a Finite Element Model of the Human Neck. Paper presented at the SAE Technical Paper Series, 1998.

4.2.9 Figures
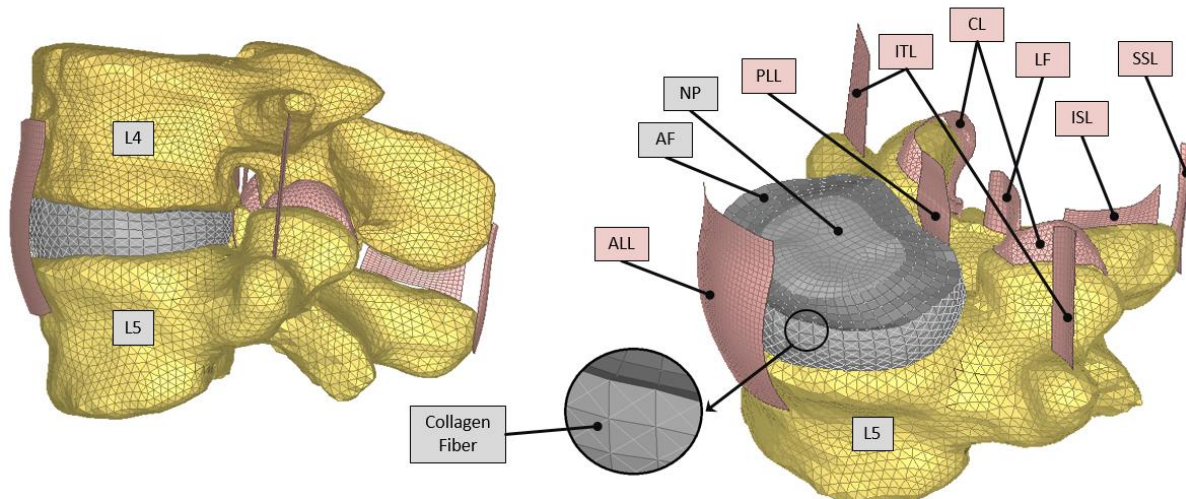
Figure 4-1 The uninstrumented FE model of the L4-L5 segment including the vertebrae, seven spinal ligaments, and intervertebral disc. ALL: Anterior Longitudinal ligament, PLL: Posterior Longitudinal Ligament, ITL: Intertransverse Ligament, CL: Capsular Ligament, LF: Ligament Flavum, ISL: Interspinous Ligament, SSL: Supraspinous Ligament, AF: Annulus Fibrosus, NP: Nucleus Pulposus
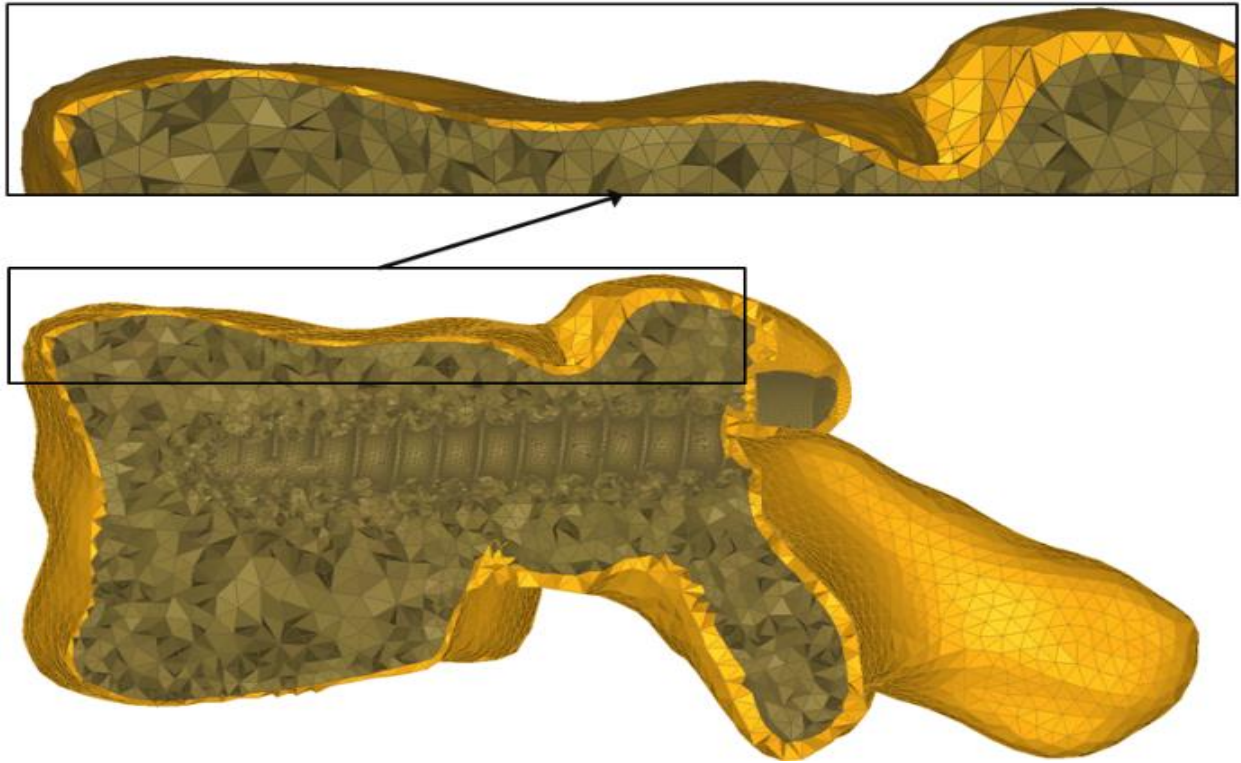
Figure 4-2 Regional thickness of the cortical bone and finer mesh of the trabecular bone around the screw imprint for L5
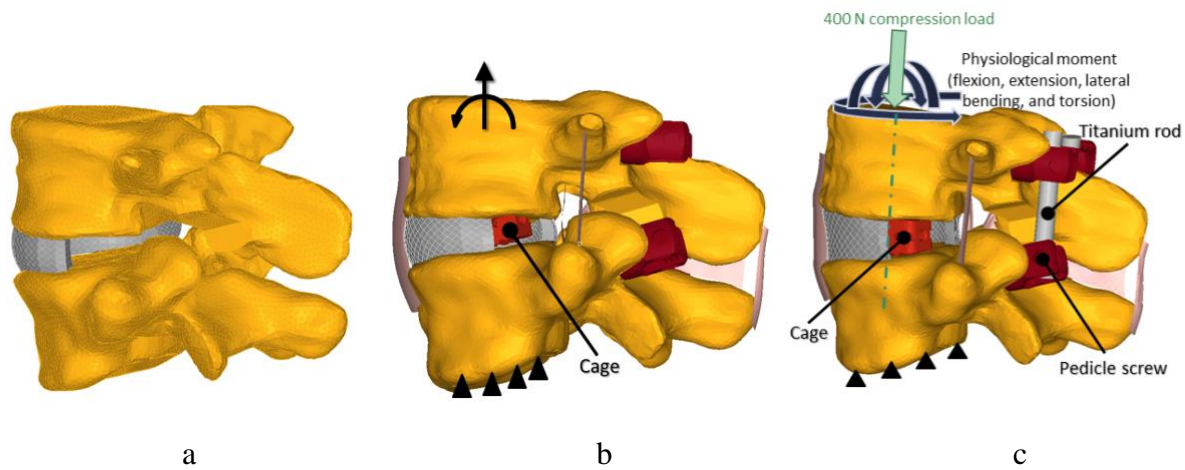
Figure 4-3 Simulation of different surgical procedures of TLIF: (a) Partial discectomy and facetectomy of L4-L5, (b) Cage placement by imposing distractive force and moment on L4, while the inferior endplate of L5 was fixed in space, and (c) Implementation of the posterior fixation followed by application of the follower load and physiological moments (flexion, extension, lateral bending, and torsion) on the superior endplate of L4 while the inferior endplate of L5 was fixed in space
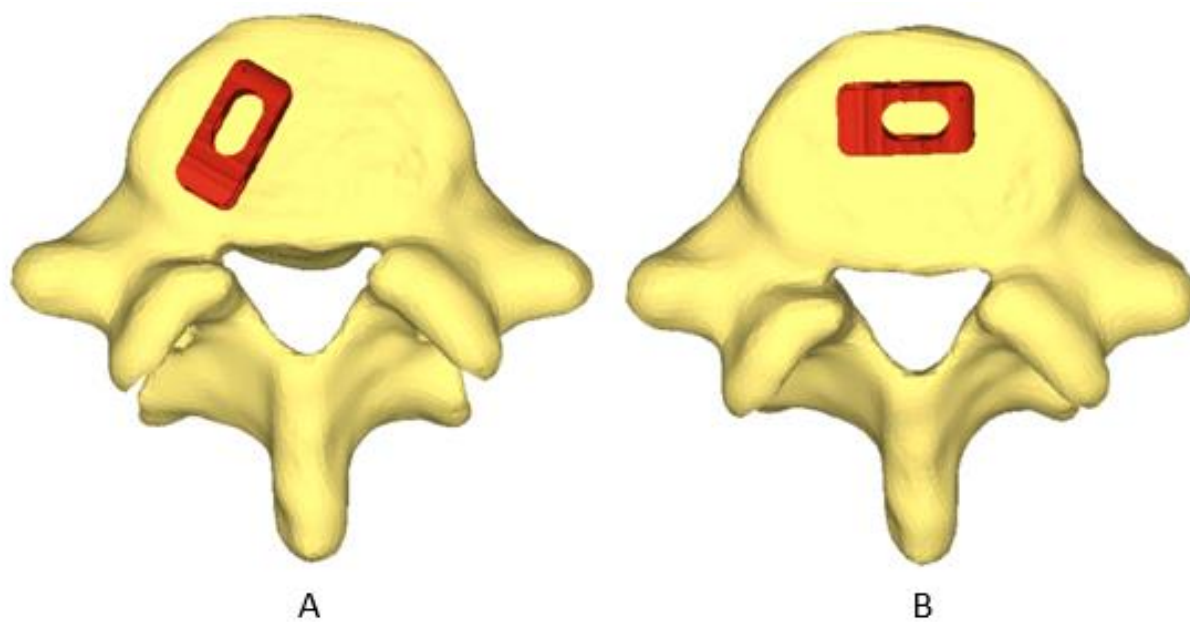
Figure 4-4 Simulated placement scenarios of the cage: (a) Oblique asymmetric: (b) Anterior symmetric
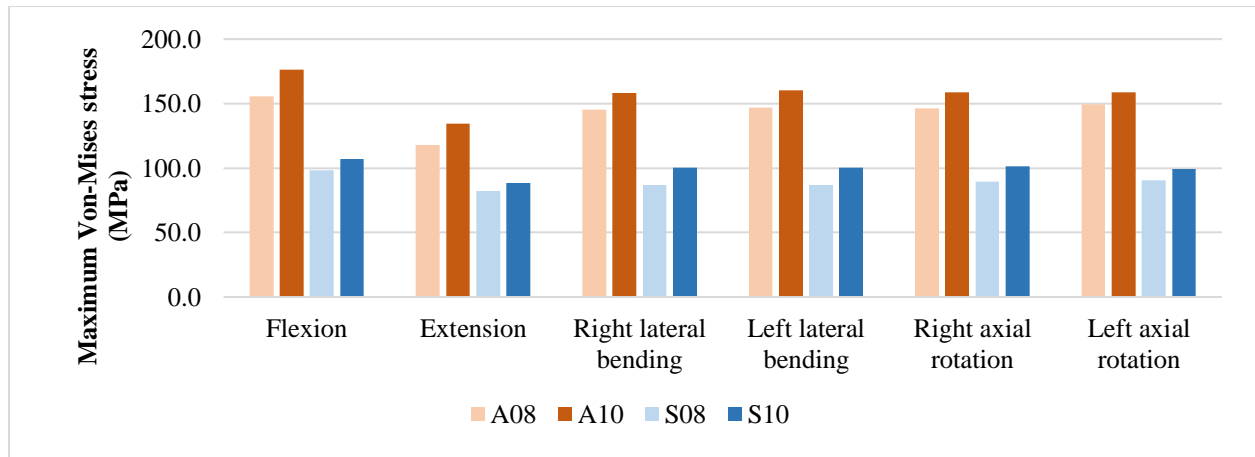
a
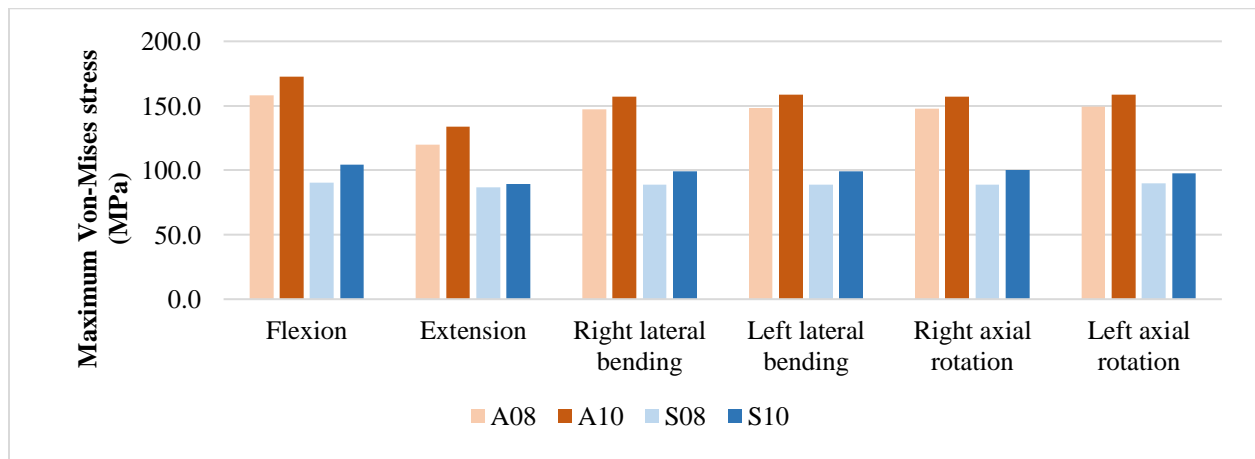
b

Figure 4-5 Maximum Von-Mises stress at the endplate-cage interface in different loading directions for normal (a) and osteoporotic (b) bone model (A08/A10: Oblique asymmetric placement of 8/10-mm cage; S08/S10: Anterior symmetric placement of 8/10-mm cage)
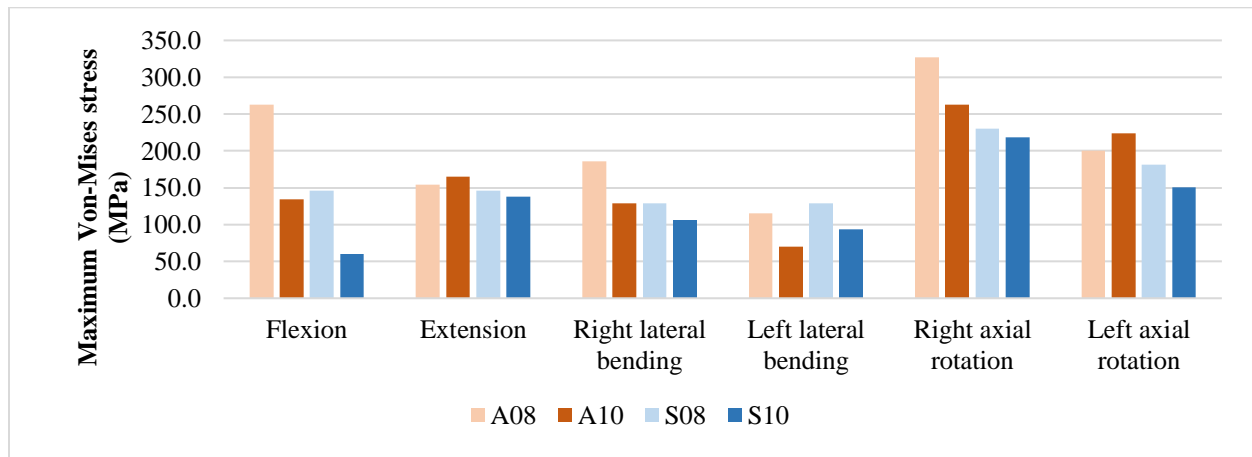
a
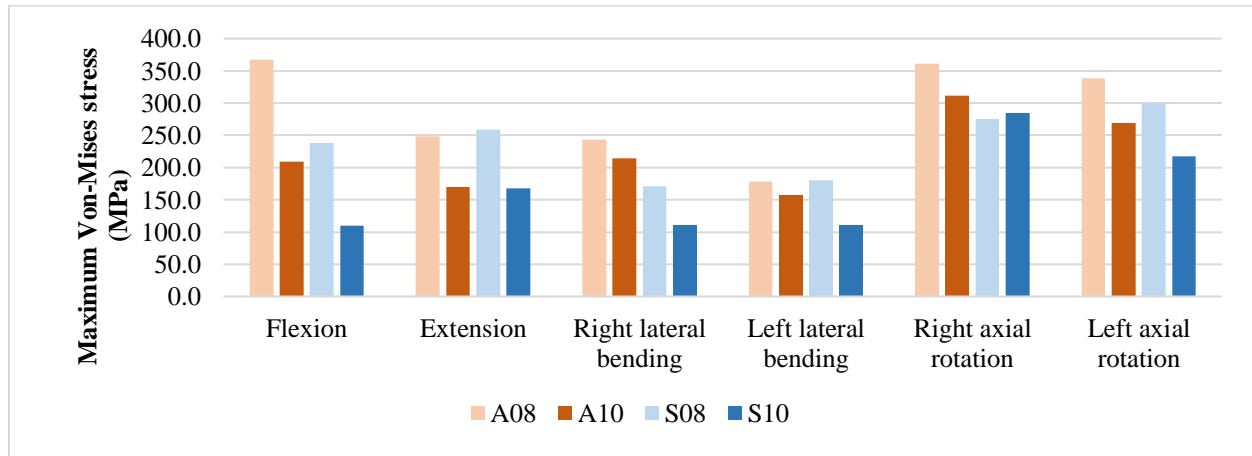
b

Figure 4-6 Maximum Von-Mises stress in the posterior rods in different loading directions for normal (a) and osteoporotic (b) bone models (A08/A10: Oblique asymmetric placement of 8/10-mm cage; S08/S10: Anterior symmetric placement of 8/10-mm cage)

4.2.10 Tables

Table 4-2 Material properties of bony elements of the FEM (from a previous cadaveric study [14])

Parameters	Cortical Bone	Trabecular Bone
Density, ρ (kg/mm^3)	2.00E-06	2.00E-07
Young's modulus, E (MPa)	2625	48.75
Poisson's ratio, v	0.3	0.25
Yield stress, a (MPa)	105	1.95
Hardening modulus, b (MPa)	875	16.3
Hardening exponent, n	1	1
Failure plastic strain, ε_{max}	0.04	0.04

Table 4-3 Material properties of the intervertebral disc

Parameter	Nucleus pulposus	Annulus matrix	Ref.
Density (kg/mm³)	1.00E-6	1.2E-06	[23]
Poisson's ratio	0.495	0.45	[29]
C_{10}	0.12	0.18	
C_{01}	0.03	0.045	

Table 4 Material properties of the ligaments (ALL: Anterior longitudinal ligament; PLL: Posterior longitudinal ligament, ITL: Intertransverse ligament, ISL: Interspinous Ligament, LF: Ligament flavum, SSL: Supraspinous ligament, and CL: Capsular ligament)

Parameter	ALL	PLL	ITL	ISL	LF	SSL	CL	Ref.
Density (kg/mm^3)	1.0E-06	1.0E-06	1.0E-06	1.0E-06	1.0E-06	1.0E-06	1.0E-06	[10]
Young modulus, E (MPa)	11.4	9.12	11.4	4.56	5.7	8.55	22.8	[36]
Poisson ratio, v	0.4	0.4	0.4	0.4	0.4	0.4	0.4	[36]
Tangent modulus, E_t (MPa)	10.0	9.0	11.0	4.0	5.0	8.0	22.0	
Tangent poisson ratio, v_t	0.42	0.42	0.42	0.42	0.42	0.42	0.42	[10]
Viscosity coefficient, η_0	28	28	28	28	28	28	28	
Navier's constant, λ	1.0E06	1.0E06	1.0E06	1.0E06	1.0E06	1.0E06	1.0E06	

CHAPTER 5   VERIFICATION, VALIDATION, AND SENSITIVITY ANALYSES

5.1 Introduction

The validation and predictive capability of the developed FEM in the context of TLIF biomechanics was assessed through a validation/verification (V&V) process, following the V&V40:2018 principles [89]. This guideline proposes to obtain the trust through the productivity of the results by gathering sufficient criteria supporting the findings. For the computational model, model form and model inputs are two factors to be tested to acquire model credibility. To do so, the model inputs, geometrical modeling, and model assumptions should be assessed in the context of use (COU) of the developed model. With this regard, we used a strategy composed of several complementary tests enabling to establish the confidence level of the results obtained from the developed FEM of TLIF.

The created SLL after the cage placement mostly resulted from the reaction of the soft tissues (i.e. the spinal ligaments); thus, the effect of behavior of the spinal ligaments on the simulating SLL were examined. To make sure that mechanical kinematics of the spinal ligaments was consistent with the available cadaveric experimental tests, two studies were conducted: 1) the ROM of the uninstrumented model was compared with the available literature; 2) the resulting SLL after the cage placement was calculated when an alternate set of Young's moduli of the ligaments was incorporated in the FEM of TLIF. This new set of Young's moduli was adapted from the literature to consider inter-variability of the spinal ligaments.

From a mechanical point of view, the maximum Von-mises stress is a criterion to compare the risk of cage subsidence between two cases. To rely on the calculated stresses, it was necessary to show that a proper mesh had been generated as well as to characterize the dependency of the stress values on the model inputs and assumptions. The proper mesh size of the cortical bone was achieved through a convergence study using the instrumented FEM, and the trabecular elements were refined accordingly. The effects of the variation of the model inputs on the model outputs were evaluated through the sensitivity analyses. The calculated Von-Mises stresses were tested to detect changes with varying input parameters. If no variation was detected, we hypothesized that the uncertainty was quantified. The maximum stress distribution on the superior endplate of L5 was visually

inspected to avoid stress concentration effect caused by any singular node. Furthermore, the local cage positioning was changed (+/-1 mm to the sides of initial position) to quantify the variation of the maximum and average stresses. Since osteoporosis weakens the bone, a higher risk of failure is expected in this condition, but the maximum stresses in the cortical bone with normal and osteoporotic bone models were in a similar range. Thus, the maximum strain in the cortical bone and maximum stress in the trabecular bone were calculated to better describe the risk of cage subsidence between normal and osteoporotic bone. The variation of the maximum and average stresses on the superior endplate of L5 was evaluated by changing the cortical bone thickness (0.3 and 0.4 mm) as well as the friction coefficient at the endplate-cage interface (from 0.1 to 0.25). The detail of each study is presented in the following sections.

5.2 ROM of the uninstrumented model under various bending moments

The ROM of the uninstrumented model was assessed under simulated pure bending moments of 8 Nm in flexion-extension, lateral bending, and axial rotation, and compared to the reported ROM of similar experimental cadaveric tests [90, 91]. In this study, we fixed the inferior endplate of L5 and applied an 8 Nm bending moment on the superior endplate of L4. Jaramillo et al. [90] used five L4-S1 cadaveric lumbar spine, fixed the sacrum and loaded the L4 with a pure bending moment of 8 Nm. In another cadaveric experimental test, Dahl et al. [91] applied an 8 Nm pure moment on the L3 segment of eight L3-S1 human spine while the sacrum was fixed. The segmental ROM of each motion segment was measured in these two cadaveric experiments.

The segmental ROM in our study was 9.3°, 7.6°, and 4.1° in flexion-extension, lateral bending, and axial rotation, respectively (Figure 5-1). Jaramillo et al. reported that the ROM at the L4-L5 motion segment was between 8.0° and 11.7° in flexion-extension, between 1.8° and 10.6° in lateral bending, and between 0.6° and 5.7° in axial rotation. Dahl et al. measured the ROM at the L4-L5 motion segment by 12.12±5.05°, 8.49±3.36°, and 4.29±1.81° in flexion-extension, lateral bending, and axial rotation, respectively.
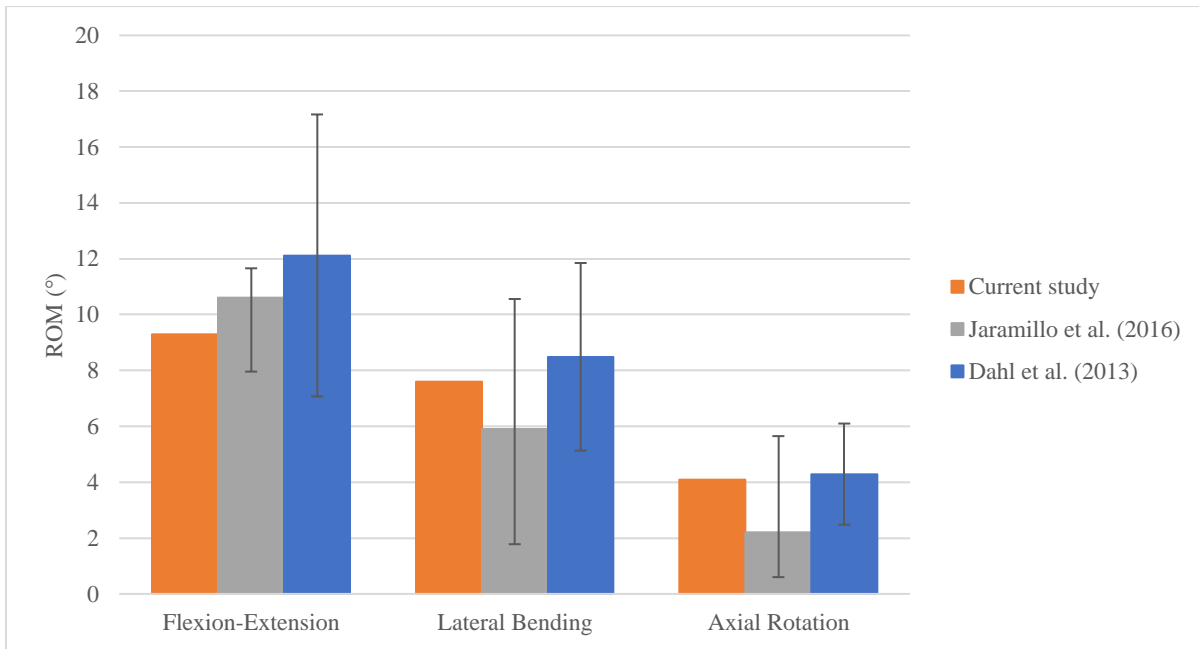
Figure 5-1 Simulated ROM under 8 Nm bending moment in flexion-extension, lateral bending, and axial rotation, and available measurements from experimental cadaveric tests

5.3 Effects of the material properties of the spinal ligaments on the resulting SLL

The created SLL was compared when two different sets of Young's modulus of the spinal ligaments were incorporated (Table 5-1). To do so, the cage insertion was simulated after the intervertebral disc preparation and partial facetectomy. In addition to the material properties used in our current study, the Young's modulus' of the spinal ligaments were adapted from the literature and were integrated in the FEM to calculate the achieved SLL [84]. The resulted SLLs from the FEM in the master thesis study were compared with those of the alternative properties.

The simulated SLL with the alternate set of Young's modulus increased by about 0.1° (between 6% and 11%) as compared to the SSL with the set of Young's modulus used in the master thesis study (Table 5-2).

Table 5-1 The Young's modulus (MPa) tested for the sensitivity analysis were adapted from the finite element study of Li et al. (2015) [84]

		The spinal ligaments						
		ALL	PLL	ITL	ISL	LF	SSL	CL
Material properties set	**Young modulus used in the master thesis study**	11.4	9.12	11.4	4.56	5.7	8.55	22.8
	Alternate Young modulus [84]	7.8	10	10	10	15	8	7.5

Table 5-2 Increment of the simulated SLL with the alternate Young's modulus' adapted from the finite element study of Li et al. (2015) [84]

		Increment of SLL			
		08-mm oblique asymmetric	08-mm anterior symmetric	10-mm oblique asymmetric	10-mm anterior symmetric
Material properties set	**Young modulus used in the master thesis study**	0.9°	1.0°	1.4°	1.7°
	Alternate Young's modulus' [84]	1.0°	1.1°	1.5°	1.8°

5.4 Mesh convergence study at the endplate-cage interface

A mesh convergence study at the endplate-cage interface of the oblique asymmetric placement of 10-mm cage was conducted to identify the proper element size. The element size of the cortical bone was changed from 0.5 mm to 1.5 mm, and the element size of the trabecular accordingly (Figure 5-2). Then, the instrumented model was subjected to a 400 N follower load and a 10 Nm bending moment. The proper element size (i.e. 1.0 mm) was chosen when the difference of the resulting maximum Von-Mises stresses at the endplate-cage interface was below 5% (Figure 5-3).

A   B   C
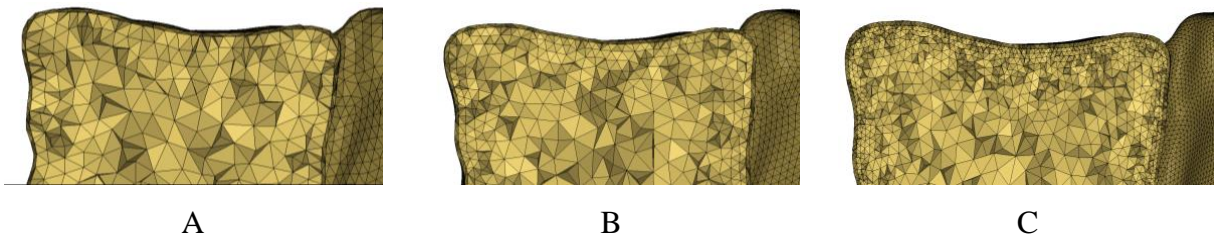
Figure 5-2 Cross sections of the L5 vertebral body with the element sizes of 1.5 (A), 1.0 (B), and 0.5 (C) mm
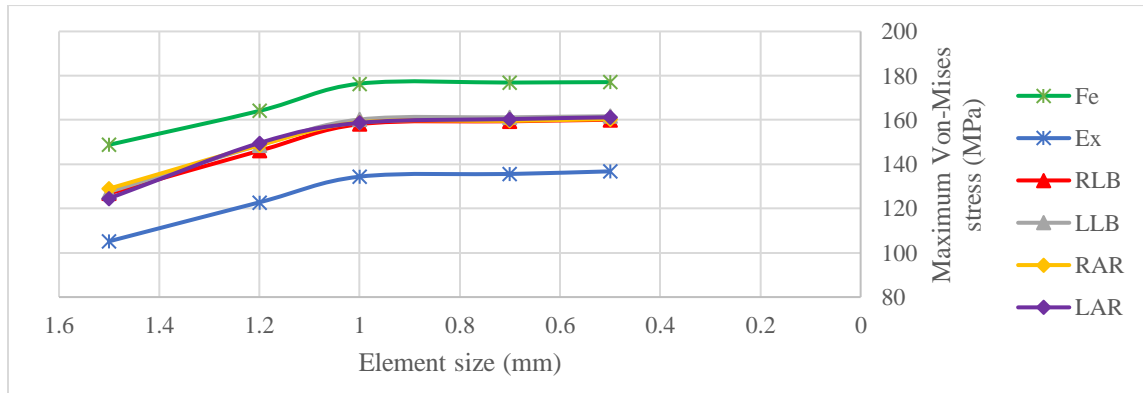
Figure 5-3 The convergence curves of the maximum stress on the superior endplate of L5 in different loading directions. The 10-mm cage was inserted in oblique asymmetric placement, the posterior fixation was conducted, and a 400 N follower load and a 10 Nm bending moment were applied. Fe: Flexion, Ex: Extension, RLB: Right Lateral Bending, LLB: Left Lateral bending, RAR: Right Axial Rotation, and LAR: Left Axial Rotation

The stress maps on the superior endplate of L5 with 3 tested element sizes (0.5, 1.0, and 1.5 mm) when the 10-mm cage was inserted oblique asymmetrically were compared. The results show that the stress distribution with 0.5- and 1.0-mm element size were similar; With the 1.5 element size, the stress was concentrated in the posterior left of the superior endplate of L5 (Figure 5-4). The calculation time of the instrumented model was about 160 min, 720 min, and 2500 min with 1.5, 1.0, and 0.5 mm element size, respectively.

A   B   C
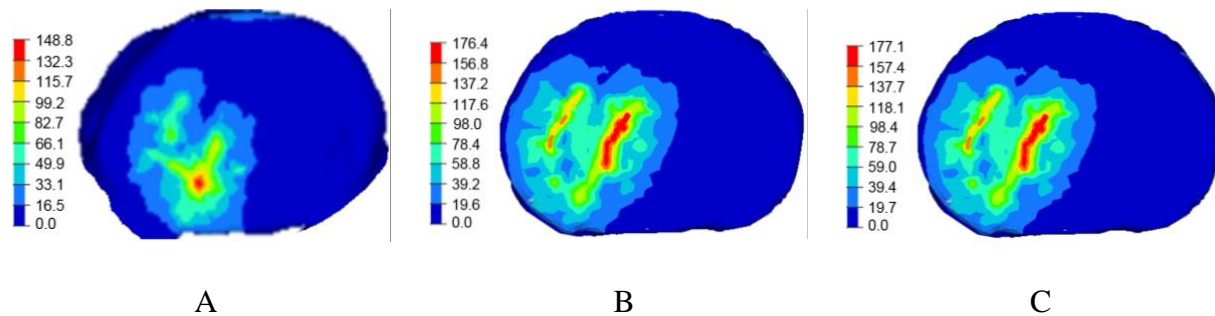
Figure 5-4 Stress maps on the superior endplate of L5 with the element sizes of 1.5 (A), 1.0 (B), and 0.5 (C) mm. The 10-mm cage was inserted in oblique asymmetric placement, the posterior instrumentation was performed, and a 400 N follower load and 10 Nm flexion moment was applied

5.5 Stress distribution at the endplate-cage interface

The CAPSTONE® cage has jagged (zig-zag) surfaces in contact with the endplates (Figure 5-5). The model of the contact interface and quality of the mesh might cause stress concentration due to local model definition such as singular nodes. The stress distribution at the endplate-cage interface was visually evaluated to determine if there was any stress concentration. The stress maps represent the maximum stresses on the superior endplate of L5 at the endplate-cage interface for the configuration with the highest magnitude of the maximum Von-Mises stress after the oblique asymmetric placement of the 10-mm cage. The maps were driven after simulation of cage insertion and posterior fixation, and application of the combination of 400 N follower load and 10 Nm bending moment in flexion (Figure 5-6). The stress maps showed that, after cage placement, the

stress was distributed around the prominences of the cage, and it was expanded across the endplate-cage interface.

<center>A   B</center>
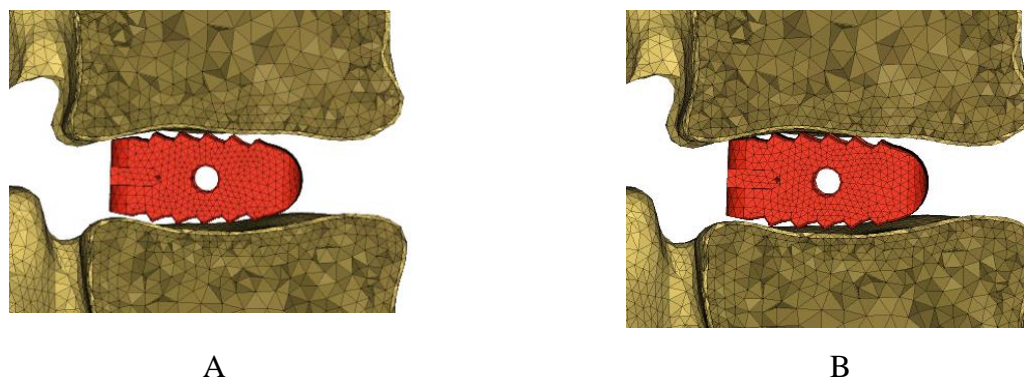
Figure 5-5 Endplates-cage interface A) after oblique asymmetric placement of the 10-mm cage with a fit contact, and B) when the posterior instrumentation was performed and segment was subjected to a combination of a 400 N follower load and flexion bending moment. Here, the mesh size is 1.0 mm

<center>A   B</center>
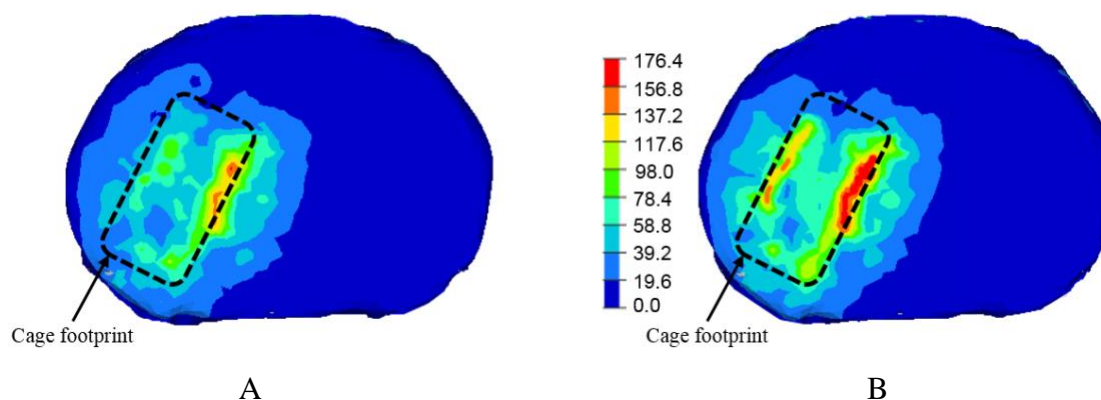
Figure 5-6 A) Stresses maps on the superior endplate of L5 after oblique asymmetric placement of the 10-mm cage, and, B) after application of the combination of the 400 N follower load and 10 Nm bending moment in flexion

5.6 Maximum stress in the trabecular bone of the L5 vertebral body

In this master project, we compared the maximum stress at the endplate-cage interface (cortical layer) between the normal and osteoporotic bone models. The results of the osteoporotic bone model (cortical layer) was identical to the normal one. Here, we calculated the maximum Von-Mises stress distribution of the trabecular bone of L5 vertebral body close to the endplate-cage interface.

For the simulated normal bone quality, with the use of 8-mm, the maximum stresses at the trabecular bone of the L5 vertebral body ranged from 2.2 to 2.5 MPa (anterior symmetric placement) and from 3.2 to 4.1 MPa (oblique asymmetric placement). With the use of 10-mm cage, they were from 2.8 to 3.8 MPa (anterior symmetric placement) and between 3.7 and 4.5 MPa (oblique asymmetric placement). For simulated osteoporosis, with the use of 8-mm, the maximum stresses at the trabecular bone of the L5 vertebral body ranged from 2.4 to 2.9 MPa (anterior symmetric placement) and from 3.7 to 4.7 MPa (oblique asymmetric placement). With the use of 10-mm cage, they were from 3.8 to 4.6 MPa (anterior symmetric placement) and between 4.3 and 5.0 MPa (oblique asymmetric placement). The stresses in the simulated osteoporosis with the insertion of 8-mm cage increased up to 18.9% and 31.8% in anterior symmetric and oblique asymmetric placement, respectively. They increased with the insertion of 10-mm cage up to 20.5% and 46.4% in anterior symmetric and oblique asymmetric placement, respectively.

5.7 Maximum strain at the endplate-cage interface

To compare the risk of cage subsidence between the normal and osteoporotic bone models, the maximum strains in the cortical layer were calculated. To do so, each interbody cage (8- and 10-mm) was inserted in oblique asymmetric and anterior symmetric orientation. Then, the instrumented segment was subjected to the 400 N follower load and 10 Nm bending moment to simulate flexion.

For the simulated normal bone quality, with the use of 8-mm, the maximum strains at the cortical bone of the L5 vertebral body were 2.78% (anterior symmetric placement) and 1.67% (oblique

asymmetric placement). With the use of 10-mm cage, they were 2.83% (anterior symmetric placement) and 1.80% (oblique asymmetric placement). For simulated osteoporosis, with the use of 8-mm cage, the maximum strains at the cortical bone of the L5 vertebral body were 3.64% (anterior symmetric placement) and 2.87% (oblique asymmetric placement). With the use of 10-mm cage, they were 4.03% (anterior symmetric placement) and 3.14% (oblique asymmetric placement). The strains in the simulated osteoporosis bone with the insertion of 8-mm cage increased by 31% and 71% in anterior symmetric and oblique asymmetric placement, respectively. They increased with the insertion of 10-mm cage by 43% and 75% in anterior symmetric and oblique asymmetric placement, respectively.

5.8 Effect of the interbody cage positioning on the stresses at the endplate-cage interface

Since the endplates have a concave profile and the interbody cage selected in this project has convex faces, the calculated stresses at the interface of the endplates might be affected by the position of the cage. To test how it could affect the resulting stresses at the endplate-cage interface, the interbody cage placement was analyzed. The 10-mm cage in oblique asymmetric placement was chosen because it had the highest maximum stress among the previously tested scenarios. The interbody cage was sequentially moved 1 mm to the left, right, front and back of its initial position (Figure 5-7). Then, for each model, the inferior endplate of L5 was fixed, and 400 N follower load was applied to the L4 followed by the 10 Nm bending moment in the physiological planes. The maximum and average stresses on the superior endplate of L5 were calculated.
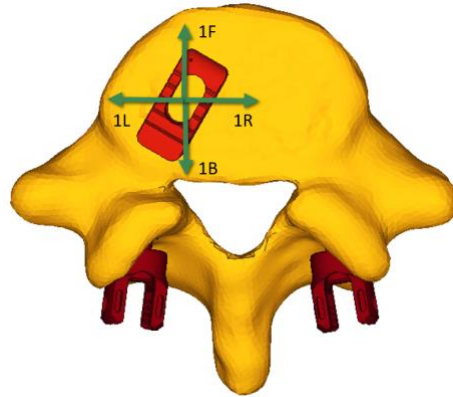
Figure 5-7 The 10-mm cage in oblique asymmetric placement was sequentially moved 1 mm to the left (1L), right (1R), front (1F), and back (1B) of its initial position. Then, for each model, the inferior endplate of L5 was fixed, and 400 N follower load was applied to the L4 followed by the 10 Nm bending moment in the physiological planes. The maximum and average stresses on the superior endplate of L5 were calculated

The maximum and average stresses at the endplate-cage interface varied from -6.9% to +8.0% and from -2.2% to +2.3%, respectively, when the cage was shifted by +/-1 mm to the sides of its initial position (Table 5-3). The variation of the maximum stress highlights the effect of cage positioning on the stress distribution at the endplate-cage interface.

Table 5-3 Maximum and average stresses (MPa) on the superior endplate of L5 when 10-mm oblique asymmetrically inserted cage was shifted 1 mm to the left, right, front and back

		Reference FEM	Cage shifted 1mm in the 4 directions and % difference with respect to the Reference			
			Back	Front	Left	Right
Flexion	**Maximum stress (% of the change)**	176.4	164.3 (-6.9%)	164.5 (-6.7%)	169.2 (-4.1%)	170.1 (-3.5%)
	Average stress (% of the change)	153.4	150.2 (-2.1%)	150.6 (-1.8%)	151.6 (-1.1%)	151.7 (-1.1%)
Extension	**Maximum stress (% of the change)**	134.4	129.9 (-3.3%)	133.9 (-0.4%)	145.2 (+8.0%)	139.2 (+3.6%)
	Average stress (% of the change)	117.8	116.3 (-1.3%)	118.3 (+0.4%)	120.5 (+2.3%)	118.7(+0.8%)
Right lateral bending	**Maximum stress (% of the change)**	158.1	147.1 (-7.0%)	151.9 (-3.9%)	150.9 (-4.6%)	149.9 (-5.2%)
	Average stress (% of the change)	135.3	132.6 (-2.0%)	133.8 (-1.1%)	132.9 (-1.8%)	134.1 (-0.9%)
Left lateral bending	**Maximum stress (% of the change)**	160.2	148.1 (-7.6%)	152.1 (-5.1%)	151.5 (-5.4%)	157.4 (-1.7%)
	Average stress (% of the change)	138.3	135.2 (-2.2%)	136.3 (-1.4%)	135.9 (-1.7%)	138.2 (-0.1%)
Right axial Rotation	**Maximum stress (% of the change)**	158.9	151.0 (-5.0%)	150.5 (-5.3)	152.5 (-4.0%)	155.6 (-2.1%)
	Average stress (% of the change)	134.5	132.6 (-1.4%)	132.5 (-1.5%)	132.8 (-1.3%)	133.3 (-0.9%)
Left axial Rotation	**Maximum stress (% of the change)**	158.7	149.8 (-5.6%)	153.2 (-3.5%)	150.6 (-5.1%)	159.4 (-0.4%)
	Average stress (% of the change)	139.8	137.6 (-1.6%)	138.4 (-1.0%)	137.7 (-1.5%)	140.1 (+0.2%)

5.9 Effect of the cortical shell thickness on the stresses at the endplate-cage interface

The thickness of the cortical shell of the vertebral body in this master project study was uniformly set to 0.4 mm, based on reported morphological measurements between 0.27 to 0.44 mm [92]. Therefore, the cortical thickness was alternately changed to 0.3 mm to assess how the maximum and average Von-Mises stresses would change. The study was done for the oblique asymmetric placement of the 10-mm cage under the combination of the 400 N follower load and 10 Nm bending moment simulating flexion, extension, lateral bending, and axial rotation. The maximum and average stresses increased up to 2.6% and 5.1%, respectively with the thickness of 0.3 vs. 0.4 mm (Table 5-4).

Table 5-4 The maximum and average Von-Mises stresses distributed on the superior endplate of L5 with two thickness of the cortical shell (0.3 and 0.4 mm)

	Maximum Von-Mises stress (MPa)		Average Von-Mises stress (MPa)	
	Thickness		Thickness	
	0.4 mm (Ref.)	0.3 mm	0.4 mm (Ref)	0.3 mm
Flexion	176.4	181.0	153.4	161.2
%Δ	--	2.6%	--	5.1%
Extension	134.4	136.7	117.8	121.2
%Δ	--	1.7%	--	2.9%
Right lateral bending	158.1	161.6	135.3	139.6
%Δ	--	2.2%	--	3.2%
Left lateral bending	160.2	163.8	138.3	142.6
%Δ	--	2.2%	--	3.1%
Right axial rotation	158.9	162.4	134.5	138.7
%Δ	--	2.2%	--	3.1%
Left axial rotation	158.7	162.2	139.8	144.2
%Δ	--	2.2%	--	3.1%

5.10 Effect of the friction coefficient at the endplate-cage interface

The friction coefficient of the endplate-cage interface governs the stress distribution at the contact area and depends on many parameters such as the surface finishing of implant and the type of materials in contact. For the PEEK and bone contact, an experimental measurement showed that the friction coefficient varied between 0.1 and 0.25 [93]. Therefore, we evaluated how the maximum and average stresses on the superior endplate of L5 varied as a function of the coefficient of friction. For this purpose, the instrumented FEM with oblique asymmetric placement of the 10-mm cage and posterior fixation was subjected to a 400 N follower load and a 10 Nm bending moment. The coefficient friction was changed alternatively (0.1, 0.14, 0.17, 0.2, 0.23, and 0.25) to calculate the maximum and average Von-Mises stresses.

The maximum stress ranged from 176.1 to 176.7 MPa (176.5±0.2 MPa), the average stress ranged from 153.2 to 153.5 MPa (153.4±0.1 MPa), and the tangent force at the endplate-cage interface was between 2.24 and 2.36 N (2.3±0.05 N) (Table 5-5).

Table 5-5 Variation of the average and maximum stresses, and tangent forces generated on the superior endplate of L5 versus different values of friction coefficient at the endplate-cage interface

Coefficient of friction	0.1	0.14	0.17	0.2	0.23	0.25
Average stress (MPa)	153.2	153.4	153.5	153.4	153.5	153.4
Maximum stress (MPa)	176.1	176.3	176.7	176.4	176.7	176.7
Tangent force (N)	2.24	2.27	2.28	2.31	2.34	2.36

5.11 Summary

The model credibility was quantified by testing the model output when the model inputs and assumptions changed (Table 5-6). The ROM of the uninstrumented model was within the reported range in the literature. Although this finding may show that the model kinematic was consistent with the literature, it does not solely confirm the model validity. Nevertheless, the calculated SLL with the alternate Young's modulus of the spinal ligaments changed about 0.1° which may infer that these input parameters do not change our predictions.

The proper mesh sizes for the cortical bone and accordingly for the trabecular bone were obtained from the convergence study. Two tests confirmed that there was no singular node at the endplate-cage interface. First, the stress distribution at the interface was visually inspected and showed that there was no stress concentration at the interface, which approve the smooth mesh generation. Second, the average Von-Mises stresses at the interface (129.9 to 170.1 MPa) were close to the maximum stresses (134.4 to 176.4 MPa) implying that there was no singular node, which generates a local stress concentration. The maximum Von-Mises stresses varied in a range of 15%, but the average was changed up to 5% with shifting the cage 1 mm to the sides with respect to the initial position. This showed that reported maximum stresses were sensitive to the cage placement, however, the variation is applicable to all the results and does not change our prediction considering that this is a comparative study. Decreased cortical thickness increased the maximum and average stresses at the interface. This is expected from a mechanical stand point, but our prediction between two placement scenarios is still similar. The maximum and average Von-Mises stresses at the interface changed slightly with different values of the coefficient of friction. The Von-Mises stress has two volumetric and deviatory parts which respectively represent the compressive and shear forces. The compressive forces were constant as we performed the tests within the similar FEMs in terms of geometry, and only the coefficient of friction at the endplate-cage interface changed. Our calculated stresses confirmed that the shear forces were identical to the coefficient of friction that may generate similar reaction friction at the interface.

The presented tests together demonstrated the ability of the FEM in the context of TLIF to compare the risk of cage subsidence with two cage heights, two placement strategies in the normal and osteoporotic bone models.

Table 5-6 Summary of the conducted tests to establish the model credibilish and to identify the uncertainty of the results corresponding to the changing model inputs and assumptions

Input	Range	Output	Range	Δ
Young's modulus of spinal ligaments	Our study (Ref.) Alternate values	Change of SLL	0.9°-1.7° 1.0°-1.8°	-- 0.1°
Element size	1.5 mm 1.0 mm (Ref.) 0.5 mm	Maximum Von-Mises stress in cortical bone	105.5-148.8 MPa 134.4-176.4 MPa 136.8-177.1 MPa	-22% to -16% -- +1% to 2%
Bone quality	Normal Osteoporosis	Maximum stress in trabecular bone	2.2-4.5 MPa 2.4-5.0 MPa	18.9% - 46.4%
Bone quality	Normal Osteoporosis	Maximum strain in cortical bone	1.67%-2.83% 2.87%-4.03%	31% - 75%
Cage placement	Initial position (Ref.) +/-1 shift	Maximum Von-Mises stress in cortical bone	134.4-176.4 MPa 129.9-170.1 MPa	-- -6.9% - 8.0%
Cage placement	Initial position (Ref.) +/-1 shift	Average Von-Mises stress in cortical bone	117.8-153.4 MPa 116.3-151.7 MPa	-- -2.2% - +2.3%
Cortical thickness	0.4 mm (Ref.) 0.3 mm	Maximum Von-Mises stress in cortical bone	134.4-176.4 MPa 136.7-181.0 MPa	-- up to +2.6%
Cortical thickness	0.4 mm (Ref.) 0.3 mm	Average Von-Mises stress in cortical bone	117.8-153.4 MPa 121.2-161.2 MPa	-- up to +5.1%
Coefficient of friction	0.2 (Ref.) 0.1-0.25	Maximum Von-Mises stress in cortical bone	176.4 MPa 176.1-176.7 MPa	-- -0.1% - +0.1%
Coefficient of friction	0.2 (Ref.) 0.1-0.25	Average Von-Mises stress in cortical bone	153.4 MPa 153.2-153.5 MPa	-- -0.2% - +0.2%
Coefficient friction	0.2 (Ref.) 0.1-0.25	Shear force at the interface	2.31 N 2.24-2.36 N	-- -3.0% - +2.1%

CHAPTER 6   GENERAL DISCUSSION

In this project, the created SLL and biomechanics of cage subsidence were investigated to evaluate the effects of two essential parameters related to the cage, namely the cage height and placement strategy. A finite element model of the L4-L5 motion segment of the spine was adapted to simulate the TLIF procedure with the use of two different cage heights (8 vs. 10 mm) in oblique asymmetric and anterior symmetric placements. The maximum and average stresses at the endplate-cage interface were calculated as a mean to relatively assess the risk of cage subsidence.

The result of this study can be used to compare the achieved SLL between two placement strategies and two selected heights. The conclusion may be used to assess which placement or cage height has advantages over its alternative, but cannot be extrapolated to the other types of interbody cages. This study simulated the early postoperative situation in prone position, and we expect different values for standing in which the clinical studies measured the SLL. In addition, the risk of cage subsidence was analyzed when the cage height and its placement were changed in simulated normal and osteoporosis models. The cage subsidence was reported even more than 30% after 1st- and 2nd-year follow-up [4], which is a remarkable incidence. These results can be used to evaluate the relative difference between each pair of models and cannot be considered as the absolute values. This enable us to decide which placement or which height of cage relatively generates lower maximum stress, which may have the lowest risk of cage subsidence.

The calculated SLL (up to 1.7°) was consistent with the reported value (1.8°) [94] in the literature when unilateral partial facetectomy was performed in TLIF. A higher simulated SLL was achieved with the use of 10-mm vs. 8-mm cage. This result was expected from a geometrical point of view as the insertion of a thicker cage requires more distraction of the intervertebral disc space, which leads to a higher SLL. As a consequence, with the insertion of a thicker cage, a higher reaction force initiated at the endplate-cage interface by the stretched spinal ligaments and soft tissues. As the compression force at the endplate-cage interface increases, a higher stress distribution was generated, which may produce a higher risk of cage subsidence. The average and maximum stresses at the endplate-cage interface consistently support this expectation.

The simulated SLL with anterior symmetric placement was very similar to the oblique asymmetric placement, but the average and maximum stresses were lower, which could be inferred as a lower risk of cage subsidence. This can be attributed to the fact that the cage acts as a pivot center, around

which the upper vertebra (L4) rotates in presence of bending moments. Symmetric anterior placement of the cage vs. the oblique asymmetric position relatively increases the lever arm of the compressive forces from the tested functional loads. Similarly, reported *in* vivo measurements revealed that the anterior region of the vertebral endplates has a superior maximum failure load as compared to the lateral and more posterior area (751 ± 24 vs. 596 ± 75 N [95]).

The oblique asymmetric placement increased not only the stress distribution at the endplate-cage interface, but also the stresses at the posterior rods, which implies a higher risk of rod failure. In anterior symmetric placement of the cage, the posterior rods have a higher lever arm with respect to the cage (pivot point), thus a lower load was required to balance the transferred loads to the spinal segment. The lower transferred loads to the posterior rods, again, infer that anterior symmetric placement of cage has better mechanical advantages to decrease the risk of rods failure as well as the risk of cage subsidence.

The maximum stresses in the endplates with the simulated material properties of the osteoporotic bone were almost similar to those with the simulated normal bone. Higher risk of cage subsidence is expected with the osteoporotic bone as bone density can be reduced up to 30% compared to the normal asymptomatic bone [96]. The maximum stresses in the trabecular bone were higher in the osteoporosis model, which confirms that failure of trabecular bone may lead to cage subsidence. Therefore, from a mechanical point of view, a bigger endplate-cage footprint would help to distribute the compressive force across a wider area leading to a lower magnitude of the pressure. The aforementioned consideration was shown in the reported work of Faizan et al. (2015) where a 75% larger footprint of the cage reduced the peak stress up to 50%, resulting to a lower risk of cage subsidence [7].

The V&V and sensitivity analysis quantified the uncertainty associated with the model inputs and assumptions based on the ASME V&V-40. The ROMs of the motion segment of the FEM in physiological planes were within the range reported in the experimental cadaveric studies [90, 91]. The resulted SLL with the alternative elastic modulus' of the spinal ligament was identical to that of this master study. Generated mesh of the cortical vertebral body was refined as well as the trabecular bone, accordingly. The calculated average and maximum stresses at the endplate-cage interface were sensitive to the placement of the cage (15% for the peak stress, but 5% for the

average pressure for small displacements +/- 1 mm). The average stresses at the endplate-cage interface were very small, while the variation in the maximum stresses could be attributed to the local positioning of the cage. The convergence study, the assessment of the stress distribution at the endplate-cage interface, and the variation of the average stresses (less than 5%) with +/-1 mm local placement confirms the quality of the mesh meaning this variation does not result from the singular nodes. The maximum stress at the endplate-cage interface in cortical bone was slightly higher with the modeled normal bone vs. osteoporosis, however, the maximum stresses in the trabecular bone increased in the osteoporosis bone. This may imply that compromised trabecular bone increases the risk of cage subsidence in osteoporosis. The sensitivity analysis also revealed a small difference in the average and maximum stresses with the thickness of the cortical shell, and coefficient friction. The developed FEM in this master project can be further extended to study multilevel TLIF, analyze the biomechanics of posterior fixation in TLIF, and understand the mechanism of adjacent segment degeneration (ASD).

This finite element study, as for most numerical models and analyses, has some inherent limitations. Firstly, the calculated results are restricted by the absence of the muscle forces; however, the follower load mimicked the upper bodyweight and muscular stabilization as a mitigation [7]. The follower load was applied along the current curvature of the segment which simulated the loading mode in standing posture with stabilizing transverse forces [97]. As we reported relative differences between the tested parameters, the effects of the simplified stabilizing muscle forces would be constant throughout the simulated scenarios. The same argument applies with another limitation of the study (e.g. the thickness and material properties of the cortical bone of the vertebral body), which is the only one tested asymptomatic 50th percentile spine geometry. In a future study, the FEM could be adapted to test different spinal shapes and sagittal profiles with a similar protocol. In this study, we analyzed a constant posterior fixation strategy in order to solely assess the effects of the tested interbody parameters, namely height of cage and its placement strategy. We have not tested different decompression procedures of the segment and also compression of the posterior elements, as could be done by surgeons, which could possibly further influence the level of SLL restoration. Finally, the current study only addressed one level TLIF procedure at L4-L5. The biomechanics of multilevel TLIF might be a future study aiming to assess more complex surgical procedures.

Putting together the knowledge gained in this master research study and current state-of-art in biomechanics of TLIF, the following subjects would be of interest for further investigations:

i. Pullout strength of the pedicle screws in TLIF as a function of the screw insertion (orientation) and cage placement;

ii. Comparison of single and multilevel TLIF in terms of risk of cage subsidence and posterior instrumentation failure;

iii. Biomechanics of adjacent segment degeneration in TLIF with the change of key parameters such as the number of fused segments, cage placement, and curvature of the rods.

CHAPTER 7   CONCLUSIONS AND RECOMMENDATIONS

In this thesis, the biomechanics of the TLIF was investigated by the means of finite element analysis. SLL and risk of cage subsidence interpreted as a function of the induced stresses at the cage/endplate interface were evaluated with the change of cage height (8 vs. 10 mm), cage placement strategy (anterior symmetric vs. oblique asymmetric) with two simulated bone qualities (normal vs. osteoporotic). Overall, 8 models each were tested in physiological loading conditions simulating flexion, extension, lateral bending, and axial rotation.

The SLL resulting from the insertion of the 10-mm cage into the intervertebral disc space was higher than that of the 8-mm cage, but the SLL simulated with the anterior asymmetric and oblique asymmetric placements was relatively close. The resulting ROM at the L4-L5 segment after different physiological loading simulations was very limited (<1°), showing the capacity of the TLIF and of the posterior instrumentation to promote a solid fusion. The 10-mm cage resulted in higher stresses at the endplate-cage interface. Also, the oblique asymmetric placement of the cage systematically introduced higher stresses at the endplate-cage interface, as compared to the tested anterior symmetric placement. From the stress analysis of the various tested scenarios, we can infer that the cage with 8-mm height and anterior symmetric placement of the cage was the scenario with the smallest stresses, which would have the smallest risk of cage subsidence, especially in osteoporotic conditions where the bone strength to support the loads is challenging.

The developed TLIF FEM in this project was shown to be a relevant tool to perform a comparative study on the interbody cage biomechanics, suited to supplement clinical and experimental studies, to bring more insight into the assessment of the risk of cage subsidence. The modeling technique can be extended for the whole lumbar spine to investigate multilevel TLIF as well as posterior fixation biomechanics. A comprehensive validation and verification would be necessary before using the extended FEM in the context.

BIBLIOGRAPHY

[1]   V. M. Ravindra, S. S. Senglaub, A. Rattani, M. C. Dewan, R. Härtl, E. Bisson*, et al.*, "Degenerative lumbar spine disease: estimating global incidence and worldwide volume," *Global spine journal,* vol. 8, pp. 784-794, 2018.

[2]   B. M. Agrawal and D. Resnick, "Transforaminal lumbar interbody fusion: indications and techniques," in *Schmidek and Sweet operative neurosurgical techniques.*, ed Philadelphia: W.B. Saunders, 2012, pp. 1951-1954.

[3]   J. L. Gum, D. Reddy, and S. Glassman, "Transforaminal lumbar interbody fusion (TLIF)," *JBJS Essent Surg Tech,* vol. 6, p. e22, Jun 2016.

[4]   N. Lee, K. N. Kim, S. Yi, Y. Ha, D. A. Shin, D. H. Yoon*, et al.*, "Comparison of outcomes of anterior, posterior, and transforaminal lumbar interbody fusion surgery at a single lumbar level with degenerative spinal disease," *World Neurosurgery,* vol. 101, pp. 216-226, 2017.

[5]   T. V. Le, A. A. Baaj, E. Dakwar, C. J. Burkett, G. Murray, D. A. Smith*, et al.*, "Subsidence of polyetheretherketone intervertebral cages in minimally invasive lateral retroperitoneal transpsoas lumbar interbody fusion," *Spine,* vol. 37, pp. 1268-73, Jun 2012.

[6]   G. M. Malham, R. M. Parker, C. M. Blecher, and K. A. Seex, "Assessment and classification of subsidence after lateral interbody fusion using serial computed tomography," *J Neurosurg Spine,* pp. 1-9, Jul 2015.

[7]   A. Faizan, A. Kiapour, A. M. Kiapour, and V. K. Goel, "Biomechanical analysis of various footprints of transforaminal lumbar interbody fusion devices," *Journal of Spinal Disorders & Techniques,* vol. 27, pp. E118-E127, Jun 2014.

[8]   C. W. Kim, T. M. Doerr, I. Y. Luna, G. Joshua, S. R. Shen, X. Fu*, et al.*, "Minimally invasive transforaminal lumbar interbody fusion using expandable technology: a clinical and radiographic analysis of 50 patients," *World Neurosurg,* vol. 90, pp. 228-35, Jun 2016.

[9]   J.-T. Kim, M.-H. Shin, H.-J. Lee, and D.-Y. Choi, "Restoration of lumbopelvic sagittal alignment and its maintenance following transforaminal lumbar interbody fusion (TLIF): comparison between straight type versus curvilinear type cage," *European spine journal,* vol. 24, pp. 2588-96, Nov 2015.

[10]   A. Agarwal, V. Palepu, A. K. Agarwal, V. K. Goel, and E. D. Yildirim, "Biomechanical evaluation of an endplate-conformed polycaprolactone-hydroxyapatite intervertebral fusion graft and its comparison with a typical nonconformed cortical graft," *J Biomech Eng,* vol. 135, pp. 61005-9, Jun 2013.

[11]   W. Cho, C. Wu, A. A. Mehbod, and E. E. Transfeldt, "Comparison of cage designs for transforaminal lumbar interbody fusion: a biomechanical study," *Clin Biomech (Bristol, Avon),* vol. 23, pp. 979-85, Oct 2008.

[12]   Q.-X. Deng, Y.-S. Ou, Y. Zhu, Z.-H. Zhao, B. Liu, Q. Huang*, et al.*, "Clinical outcomes of two types of cages used in transforaminal lumbar interbody fusion for the treatment of degenerative lumbar diseases: n-HA/PA66 cages versus PEEK cages," *Journal of Materials Science. Materials in Medicine,* vol. 27, p. 102, 2016.

[13]   H. Xu, W. Ju, N. Xu, X. Zhang, X. Zhu, L. Zhu*, et al.*, "Biomechanical comparison of transforaminal lumbar interbody fusion with 1 or 2 cages by finite-element analysis," *Neurosurgery,* vol. 73, pp. 198-205, 2013.

[14]   D. V. Ambati, E. K. Wright, Jr., R. A. Lehman, Jr., D. G. Kang, S. C. Wagner, and A. E. Dmitriev, "Bilateral pedicle screw fixation provides superior biomechanical stability in transforaminal lumbar interbody fusion: a finite element study," *Spine J,* vol. 15, pp. 1812-22, Aug 1 2015.

[15]   S. H. Chen, S. C. Lin, W. C. Tsai, C. W. Wang, and S. H. Chao, "Biomechanical comparison of unilateral and bilateral pedicle screws fixation for transforaminal lumbar interbody fusion after decompressive surgery--a finite element analysis," *BMC Musculoskelet Disord,* vol. 13, p. 72, 2012.

[16]   E. Truumees, C. K. Demetropoulos, K. H. Yang, and H. N. Herkowitz, "Effects of disc height and distractive forces on graft compression in an anterior cervical corpectomy model," *Spine,* vol. 33, pp. 1438-41, Jun 2008.

[17]   J.-T. Kim, M.-H. Shin, H.-J. Lee, and D.-Y. Choi, "Restoration of lumbopelvic sagittal alignment and its maintenance following transforaminal lumbar interbody fusion (TLIF):

comparison between straight type versus curvilinear type cage," *European Spine Journal,* vol. 24, pp. 2588-2596, November 01 2015.

[18]   T. H. Hong, K. J. Cho, Y. T. Kim, J. W. Park, B. H. Seo, and N. C. Kim, "Does lordotic angle of cage determine lumbar lordosis in lumbar interbody fusion?," *Spine,* Oct 2016.

[19]   L. Ombregt, "Applied anatomy of the lumbar spine," in *A System of Orthopaedic Medicine*, 3rd ed: Churchill Livingstone, 2013, pp. 415-436.e4.

[20]   N. Inoue and A. A. Espinoza Orias, "Biomechanics of intervertebral disk degeneration," *Orthop Clin North Am,* vol. 42, pp. 487-99, vii, Oct 2011.

[21]   P. Dolan and M. A. Adams, "Recent advances in lumbar spinal mechanics and their significance for modelling," *Clinical Biomechanics,* vol. 16, pp. S8-S16, 2001.

[22]   M. Kurutz and L. Oroszváry, *Finite element modeling and simulation of healthy and degenerated human lumbar spine*: INTECH Open Access Publisher, 2012.

[23]   A. Nachemson and J. M. Morris, "In vivo measurements of intradiscal pressure: discometry, a method for the determination of pressure in the lower lumbar discs," *J Bone Joint Surg Am,* vol. 46, pp. 1077-92, Jul 1964.

[24]   F. Stephen, "Biomechanics of Spine," in *Spinal disorders: fundamentals of diagnosis and treatment*. vol. 1166, ed: Springer, 2008, pp. 41-66.

[25]   J. Cholewicki, K. Juluru, and S. M. McGill, "Intra-abdominal pressure mechanism for stabilizing the lumbar spine," *Journal of Biomechanics,* vol. 32, pp. 13-17, 1999.

[26]   M. Griffioen, E. Maaswinkel, W. W. A. Zuurmond, J. H. van Dieën, and R. S. G. M. Perez, "Trunk stabilization estimated using pseudorandom force perturbations, a reliability study," *Journal of Biomechanics,* vol. 49, pp. 244-251, 2016.

[27]   P. W Hodges, A. E. Martin Eriksson, D. Shirley, and S. C Gandevia, "Intra-abdominal pressure increases stiffness of the lumbar spine," *Journal of Biomechanics,* vol. 38, pp. 1873-1880, 2005.

[28]   P. A. Cripton, S. G. Kroeker, and A. Saari, "Musculature Actuation and Biomechanics of the Spine," in *Spine Technology Handbook*, ed Burlington: Academic Press, 2006, pp. 99-143.

[29]   A. Schultz, G. Andersson, R. Ortengren, K. Haderspeck, and A. Nachemson, "Loads on the lumbar spine. Validation of a biomechanical analysis by measurements of intradiscal pressures and myoelectric signals," *J Bone Joint Surg Am,* vol. 64, pp. 713-20, Jun 1982.

[30]   J. Clin, C.-É. Aubin, N. Lalonde, S. Parent, and H. Labelle, "A new method to include the gravitational forces in a finite element model of the scoliotic spine," *Medical & Biological Engineering & Computing,* vol. 49, pp. 967-977, August 2011.

[31]   A. G. Patwardhan, R. M. Havey, K. P. Meade, B. Lee, and B. Dunlap, "A follower load increases the load-carrying capacity of the lumbar spine in compression," *Spine,* vol. 24, pp. 1003-9, May 1999.

[32]   A. A. White and M. M. Panjabi, *Clinical biomechanics of the spine* vol. 2: Lippincott Philadelphia, 1990.

[33]   M. M. Panjabi, "The stabilizing system of the spine. Part II. Neutral zone and instability hypothesis," *J Spinal Disord,* vol. 5, pp. 390-6; discussion 397, Dec 1992.

[34]   M. A. Adams, B. J. Freeman, H. P. Morrison, I. W. Nelson, and P. Dolan, "Mechanical initiation of intervertebral disc degeneration," *Spine,* vol. 25, pp. 1625-36, Jul 2000.

[35]   J. P. G. Urban and S. Roberts, "Degeneration of the intervertebral disc," *Arthritis Research & Therapy,* vol. 5, pp. 120-130, 2003.

[36]   J. A. Iorio, A. M. Jakoi, and A. Singla, "Biomechanics of Degenerative Spinal Disorders," *Asian Spine J,* vol. 10, pp. 377-84, Apr 2016.

[37]   J. P. Thompson, R. H. Pearce, M. T. Schechter, M. E. Adams, I. K. Tsang, and P. B. Bishop, "Preliminary evaluation of a scheme for grading the gross morphology of the human intervertebral disc," *Spine,* vol. 15, pp. 411-5, May 1990.

[38]   L. M. Benneker, P. F. Heini, S. E. Anderson, M. Alini, and K. Ito, "Correlation of radiographic and MRI parameters to morphological and biochemical assessment of intervertebral disc degeneration," *European Spine Journal,* vol. 14, pp. 27-35, 06/26.

[39]   E. Dakwar, A. Deukmedjian, Y. Ritter, C. Dain Allred, and G. R. Rechtine Ii, "Spinal pathology, conditions, and deformities: surgical intervention," in *Pathology and Intervention in Musculoskeletal Rehabilitation*, J. E. Zachazewski, W. S. Quillen, and R. C. Manske, Eds., ed: W.B. Saunders, 2016, pp. 584-611.

[40]   G. Logroscino, L. Proietti, and E. Pola, "Spine fusion: cages, plates and bone substitutes," in *Biomaterials for Spinal Surgery*, ed: Woodhead Publishing, 2012, pp. 265-294.

[41]   A. L. Williams, M. F. Gornet, and J. K. Burkus, "CT evaluation of lumbar interbody fusion: current concepts," *AJNR Am J Neuroradiol,* vol. 26, pp. 2057-66, Sep 2005.

[42]   M. M. Panjabi, "Biomechanical evaluation of spinal fixation devices: I. A conceptual framework," *Spine,* vol. 13, pp. 1129-1134, 1988.

[43]   R. F. McLain, J. K. Burkus, and D. R. Benson, "Segmental instrumentation for thoracic and thoracolumbar fractures: prospective analysis of construct survival and five-year follow-up," *Spine J,* vol. 1, pp. 310-23, Oct 2001.

[44]   L. Wang, J. Li, H. Wang, Q. Yang, D. Lv, W. Zhang*, et al.*, "Posterior short segment pedicle screw fixation and TLIF for the treatment of unstable thoracolumbar/lumbar fracture," *BMC Musculoskelet Disord,* vol. 15, p. 40, 2014.

[45]   J. W. Brantigan, A. D. Steffee, and J. M. Geiger, "A carbon fiber implant to aid interbody lumbar fusion. Mechanical testing.," *Spine,* vol. 16, pp. S277-S282, 1991.

[46]   P. A. Cripton, G. M. Jain, R. H. Wittenberg, and L. P. Nolte, "Load-sharing characteristics of stabilized lumbar spine segments," *Spine,* vol. 25, pp. 170-9, 2000.

[47]   L. A. Ferrara and V. K. Goel, "The biomechanics of spinal fusion," *ArgoSpine News & Journal,* vol. 22, pp. 57-61, June 2010.

[48]   M. F. Gornet, F. W. Chan, J. C. Coleman, B. Murrell, R. P. Nockels, B. A. Taylor*, et al.*, "Biomechanical assessment of a PEEK rod system for semi-rigid fixation of lumbar fusion constructs," *J Biomech Eng,* vol. 133, p. 081009, Aug 2011.

[49]   A. Faizan, A. Kiapour, A. M. Kiapour, and V. K. Goel, "Biomechanical analysis of various footprints of transforaminal lumbar interbody fusion devices," *J Spinal Disord Tech,* vol. 27, pp. E118-27, Jun 2014.

[50]   P. P. Tsitsopoulos, H. Serhan, L. I. Voronov, G. Carandang, R. M. Havey, A. J. Ghanayem*, et al.*, "Would an anatomically shaped lumbar interbody cage provide better stability? An in vitro cadaveric biomechanical evaluation," *Journal of spinal disorders & techniques,* vol. 25, pp. E240-4, 2012.

[51]   P. S. Patel, D. E. Shepherd, and D. W. Hukins, "The effect of screw insertion angle and thread type on the pullout strength of bone screws in normal and osteoporotic cancellous bone models," *Med Eng Phys,* vol. 32, pp. 822-8, Oct 2010.

[52]   V. Varghese, G. Saravana Kumar, and V. Krishnan, "Effect of various factors on pull out strength of pedicle screw in normal and osteoporotic cancellous bone models," *Med Eng Phys,* vol. 40, pp. 28-38, Feb 2017.

[53]   L. B. Brasiliense, B. C. Lazaro, P. M. Reyes, A. G. Newcomb, J. L. Turner, D. G. Crandall*, et al.*, "Characteristics of immediate and fatigue strength of a dual-threaded pedicle screw in cadaveric spines," *Spine J,* vol. 13, pp. 947-56, Aug 2013.

[54]   W. S. Choi, J. S. Kim, K. S. Ryu, J. W. Hur, and J. H. Seong, "Minimally Invasive Transforaminal Lumbar Interbody Fusion at L5-S1 through a Unilateral Approach: Technical Feasibility and Outcomes," *Biomed Res Int,* vol. 2016, p. 2518394, 2016.

[55]   J. Ni, Y. Zheng, N. Liu, X. Wang, X. Fang, R. Phukan*, et al.*, "Radiological evaluation of anterior lumbar fusion using PEEK cages with adjacent vertebral autograft in spinal deformity long fusion surgeries," *Eur Spine J,* vol. 24, pp. 791-9, Apr 2015.

[56]   C. K. Lee, J. Y. Park, and H. Y. Zhang, "Minimally invasive transforaminal lumbar interbody fusion using a single interbody cage and a tubular retraction system : technical

tips, and perioperative, radiologic and clinical outcomes," *J Korean Neurosurg Soc,* vol. 48, pp. 219-224, 2010.

[57]   J. Bakhsheshian, R. Khanna, W. Choy, C. D. Lawton, A. T. Nixon, A. P. Wong*, et al.*, "Incidence of graft extrusion following minimally invasive transforaminal lumbar interbody fusion," *J Clin Neurosci,* vol. 24, pp. 88-93, Feb 2016.

[58]   J.-W. Kim, H. C. Park, S. H. Yoon, S. H. Oh, S. W. Roh, D. C. Rim*, et al.*, "A multi-center clinical study of posterior lumbar interbody fusion with the expandable stand-alone cage (Tyche® Cage) for degenerative lumbar spinal disorders," *J Korean Neurosurg Soc,* vol. 42, pp. 251-257, 2007.

[59]   K. W. Oh, J. H. Lee, J. H. Lee, D. Y. Lee, and H. J. Shim, "The correlation between cage subsidence, bone mineral density, and clinical results in posterior lumbar interbody fusion," *Clin Spine Surg,* vol. 30, pp. E683-E689, Jul 2017.

[60]   A. Rohlmann, J. Calisse, G. Bergmann, and U. Weber, "Internal spinal fixator stiffness has only a minor influence on stresses in the adjacent discs," *Spine,* vol. 24, pp. 1192-5; discussion 1195-6, Jun 1999.

[61]   T. Hikata, M. Kamata, and M. Furukawa, "Risk factors for adjacent segment disease after posterior lumbar interbody fusion and efficacy of simultaneous decompression surgery for symptomatic adjacent segment disease," *J Spinal Disord Tech,* vol. 27, pp. 70-5, Apr 2014.

[62]   C.-S. Chen, C.-K. Cheng, C.-L. Liu, and W.-H. Lo, "Stress analysis of the disc adjacent to interbody fusion in lumbar spine," *Medical engineering & physics,* vol. 23, pp. 485-493, 2001.

[63]   A. C. Jones and R. K. Wilcox, "Finite element analysis of the spine: Towards a framework of verification, validation and sensitivity analysis," *Medical Engineering & Physics,* vol. 30, pp. 1287-1304, 2008.

[64]   T. A. Burkhart, D. M. Andrews, and C. E. Dunning, "Finite element modeling mesh quality, energy balance and validation methods: A review with recommendations associated with the modeling of bone tissue," *Journal of Biomechanics,* vol. 46, pp. 1477-1488, 2013.

[65] J. M. Buckley, K. Loo, and J. Motherway, "Comparison of quantitative computed tomography-based measures in predicting vertebral compressive strength," *Bone,* vol. 40, pp. 767-774, 2007.

[66] W. M. Park, K. Kim, and Y. H. Kim, "Effects of degenerated intervertebral discs on intersegmental rotations, intradiscal pressures, and facet joint forces of the whole lumbar spine," *Computers in Biology and Medicine,* vol. 43, pp. 1234-1240, 9/1/ 2013.

[67] A. Kiapour, D. V. Ambati, R. W. Hoy, and V. K. Goel, "Effect of graded facetectomy on biomechanics of Dynesys dynamic stabilization system," *Spine,* vol. 37, pp. E581-E589, 2012.

[68] T. Zander, A. Rohlmann, and G. Bergmann, "Influence of different artificial disc kinematics on spine biomechanics," *Clinical Biomechanics,* vol. 24, pp. 135-142, 2009.

[69] J. P. Little, H. de Visser, M. J. Pearcy, and C. J. Adam, "Are coupled rotations in the lumbar spine largely due to the osseo-ligamentous anatomy?--a modeling study," *Computer methods in biomechanics and biomedical engineering,* vol. 11, pp. 95-103, 2008.

[70] H. Schmidt, F. Galbusera, A. Rohlmann, T. Zander, and H.-J. Wilke, "Effect of multilevel lumbar disc arthroplasty on spine kinematics and facet joint loads in flexion and extension: a finite element analysis," *European Spine Journal,* vol. 21, pp. 663-674, 2012.

[71] C.-I. Liu, Z. C. Zhong, H.-W. Hsu, S.-L. Shih, S.-T. Wang, C. Hung*, et al.*, "Effect of the cord pretension of the Dynesys dynamic stabilisation system on the biomechanics of the lumbar spine: a finite element analysis," *European Spine Journal,* vol. 20, pp. 1850-1858, 2011.

[72] U. M. Ayturk and C. M. Puttlitz, "Parametric convergence sensitivity and validation of a finite element model of the human lumbar spine," *Computer Methods in Biomechanics and Biomedical Engineering,* vol. 14, pp. 695-705, 2011.

[73] K. B. Higgins, D. R. Sindall, A. M. Cuitino, and N. A. Langrana, "Biomechanical Alterations in Intact Osteoporotic Spine Due to Synthetic Augmentation: Finite Element Investigation," *Journal of Biomechanical Engineering,* vol. 129, pp. 575-585, 2006.

[74]   Y. Schroeder, W. Wilson, J. M. Huyghe, and F. P. Baaijens, "Osmoviscoelastic finite element model of the intervertebral disc," *European spine journal,* vol. 15, p. 361, 2006.

[75]   S. J. Ferguson, K. Ito, and L.-P. Nolte, "Fluid flow and convective transport of solutes within the intervertebral disc," *Journal of biomechanics,* vol. 37, pp. 213-221, 2004.

[76]   M. Argoubi and A. Shirazi-Adl, "Poroelastic creep response analysis of a lumbar motion segment in compression," *Journal of biomechanics,* vol. 29, pp. 1331-1339, 1996.

[77]   A. Shirazi-Adl, "Biomechanics of the lumbar spine in sagittal/lateral moments," *Spine,* vol. 19, pp. 2407-14, 1994.

[78]   M. El-Rich, P. J. Arnoux, E. Wagnac, C. Brunet, and C. E. Aubin, "Finite element investigation of the loading rate effect on the spinal load-sharing changes under impact conditions," *J Biomech,* vol. 42, pp. 1252-62, Jun 19 2009.

[79]   M. El-Rich, E. Wagnac, P. J. Arnoux, and C. E. Aubin, "Detailed modelling of the lumbar spine for trauma applications: preliminary results," *Computer Methods in Biomechanics and Biomedical Engineering,* vol. 11, pp. 93-94, 2008/01/01 2008.

[80]   M. T. Dast, "Biomechanical response of the epiphyseal vertebral growth plate under static and cyclic compression: A finite element study," 10296188 M.Sc.A., Ecole Polytechnique, Montreal (Canada), Ann Arbor, 2014.

[81]   A. H. Dicko, N. Tong-Yette, B. Gilles, F. Faure, and O. Palombi, "Construction and validation of a hybrid lumbar spine model for the fast evaluation of intradiscal pressure and mobility," *International Science Index, Medical and Health Science,* vol. 9, pp. 134-145, 2015.

[82]   A. Chagnon, C.-É. Aubin, and I. Villemure, "Biomechanical influence of disk properties on the load transfer of healthy and degenerated disks using a poroelastic finite element model," *Journal of biomechanical engineering,* vol. 132, p. 111006, 2010.

[83]   M. J. Pearcy, "Stereo radiography of lumbar spine motion," *Acta Orthopaedica Scandinavica,* vol. 56, pp. 1-45, 1985.

[84]   J. Li, J. Shang, Y. Zhou, C. Li, and H. Liu, "Finite Element Analysis of a New Pedicle Screw-Plate System for Minimally Invasive Transforaminal Lumbar Interbody Fusion," *PLoS One,* vol. 10, p. e0144637, 2015.

[85]   E. Wagnac, P. J. Arnoux, A. Garo, M. El-Rich, and C. E. Aubin, "Calibration of hyperelastic material properties of the human lumbar intervertebral disc under fast dynamic compressive loads," *J Biomech Eng,* vol. 133, p. 101007, Oct 2011.

[86]   M. Dreischarf, T. Zander, A. Shirazi-Adl, C. M. Puttlitz, C. J. Adam, C. S. Chen*, et al.*, "Comparison of eight published static finite element models of the intact lumbar spine: Predictive power of models improves when combined together," *Journal of Biomechanics,* vol. 47, pp. 1757-1766, 2014.

[87]   S. Tang, "Comparison of posterior versus transforaminal lumbar interbody fusion using finite element analysis: Influence on adjacent segmental degeneration," *Saudi medical journal,* vol. 36, p. 993, 2015.

[88]   C. C. Lo, K. J. Tsai, Z. C. Zhong, S. H. Chen, and C. Hung, "Biomechanical differences of Coflex-F and pedicle screw fixation combined with TLIF or ALIF--a finite element study," *Comput Methods Biomech Biomed Engin,* vol. 14, pp. 947-56, Nov 2011.

[89]   ASME, "Assessing Credibility of Computational Modeling through Verification and Validation: Application to Medical Devices," ed: ASME, 2018, p. 60.

[90]   H. E. Jaramillo, C. M. Puttlitz, K. McGilvray, and J. J. Garcia, "Characterization of the L4-L5-S1 motion segment using the stepwise reduction method," *J Biomech,* vol. 49, pp. 1248-1254, May 3 2016.

[91]   M. C. Dahl, A. M. Ellingson, H. P. Mehta, J. H. Huelman, and D. J. Nuckley, "The biomechanics of a multilevel lumbar spine hybrid using nucleus replacement in conjunction with fusion," *Spine J,* vol. 13, pp. 175-83, Feb 2013.

[92]   M. J. Silva, C. Wang, T. M. Keaveny, and W. C. Hayes, "Direct and computed tomography thickness measurements of the human, lumbar vertebral shell and endplate," *Bone,* vol. 15, pp. 409-14, Jul-Aug 1994.

[93]   N. B. Damm, M. M. Morlock, and N. E. Bishop, "Friction coefficient and effective interference at the implant-bone interface," *Journal of Biomechanics,* vol. 48, pp. 3517-3521, 2015.

[94]   P. A. Robertson, W. A. Armstrong, D. L. Woods, and J. J. Rawlinson, "Lordosis Recreation in Transforaminal and Posterior Lumbar Interbody Fusion: A Cadaveric Study of the Influence of Surgical Bone Resection and Cage Angle," *Spine (Phila Pa 1976),* vol. 43, pp. E1350-e1357, Nov 2018.

[95]   T. G. Lowe, S. Hashim, L. A. Wilson, M. F. O'Brien, D. A. Smith, M. J. Diekmann*, et al.*, "A biomechanical study of regional endplate strength and cage morphology as it relates to structural interbody support," *Spine,* vol. 29, pp. 2389-94, Nov 2004.

[96]   F. Tomé-Bermejo, A. R. Piñera, and L. Alvarez-Galovich, "Osteoporosis and the Management of Spinal Degenerative Disease (I)," *The archives of bone and joint surgery,* vol. 5, pp. 272-282, 2017.

[97]   A. Rohlmann, T. Zander, M. Rao, and G. Bergmann, "Applying a follower load delivers realistic results for simulating standing," *Journal of Biomechanics,* vol. 42, pp. 1520-1526, 2009/07/22/ 2009.